Construction and Building Materials 233 (2020) 117237

Contents lists available at ScienceDirect

Construction and Building Materials

journal homepage: www.elsevier.com/locate/conbuildmat

Nano-engineering of the mechanical properties of tobermorite 14 Å with graphene via molecular dynamics simulations

B. Al-Muhit, F. Sanchez *

Department of Civil and Environment Engineering, Vanderbilt University, PMB 351831, 2301 Vanderbilt Place, Nashville, TN 37235-1831, USA

HIGHLIGHTS

- Graphene enhanced the in-plane tensile strength, stiffness, and toughness of tobermorite.
- More strengthening of graphene when interfacing with water than with solid surfaces.
- Strengthening ascribed to molecular friction with water between graphene–tobermorite surfaces.
- Influence of the interface characteristics on the mechanical behavior revealed upon loading.

ARTICLE INFO

Article history:
Received 4 June 2019
Received in revised form 23 September 2019
Accepted 12 October 2019
Available online 28 October 2019

Keywords:
Molecular dynamics
Nanocomposite
Tobermorite
Graphene
Interface
Molecular friction
Mechanical properties

ABSTRACT

The tensile and shear properties of tobermorite 14 Å-based structures reinforced with a single graphene sheet (GS) interfacing with either the surface water, octahedral calcium, or tetrahedral silicate layer were investigated using molecular dynamics simulations. The GS contributed to a significant increase in the XY-plane tensile (180%–360%) and shear (90%–225%) strengths, stiffness, and toughness while degrading the out-of-plane properties of the tobermorite structures. The water interface promoted molecular friction (intermolecular forces) and resulted in greater in-plane fracture tensile strength and toughness but a lower shear toughness than when the GS interfaced with the dry solid surfaces.

1. Introduction

Cement-based materials are inherently weak in tension. While nano- and microscale fiber reinforcements have been the method of choice for enhancing the material tensile properties by bridging cracks and improving the material load transfer capacity [1], this approach primarily addresses the material tensile property at the macroscale composite level rather than building on the molecular nature of the cement hydrates. Calcium silicate hydrate (C–S–H) is the main binding cement hydrate responsible for the tensile properties of cement-based materials [2]. Nanotechnology offers the opportunity for the development of new C–S–H nanocomposites [3,4]. Nano-engineering of C–S–H through the grafting of graphene-based materials can be a viable option for enhancing the tensile capacity of cement-based materials. A literature review on research progress of graphene reinforced cement-based composites can be found in [5].

While experimental techniques, including atomic force microscopy and nanoindentation mapping, are capable of studying the mechanical properties of cement phases [6,7], these techniques provide microscale information from which nanoscale behavior must be deduced, and no molecular level detail of the internal, cohesive forces are obtained. Molecular dynamics (MD) modeling provides a useful tool for understanding atomistic scale, reinforcing mechanisms and tuning the mechanical properties of C–S–H. MD has been successfully used to investigate the structural and mechanical properties of C–S–H at the molecular scale, including its tensile and shear strengths [8–12]. MD studies of the mechanical response of C–S–H with embedded carbon nanotubes, graphene, and graphene derivatives have been recently reported in the literature [13–18]. While factors such as calcium to silicon

* Corresponding author.
E-mail address: florence.sanchez@vanderbilt.edu (F. Sanchez).

https://doi.org/10.1016/j.conbuildmat.2019.117237
0950-0618/

(Ca/Si) ratio, connectivity of the silicate chains, non-bridging oxygen sites, and hydrolytic reactions have been found to influence the interactions between C–S–H and graphene derivatives [12,14,19], little is known, however, about the possible influence of the interface composition and structure on the strengthening mechanisms and mechanical properties of reinforced C–S–H nanocomposites. Yet, the formation of multiple interfaces with different chemistry and structures between graphene and C–S–H are expected in cement systems as a result of heterogeneous nucleation and growth of C–S–H on the graphene surface [20]. Different S–H phases will have different interactions with the graphene surface through distinct interfaces that contribute simultaneously to the overall mechanical properties of carbon-reinforced cements. However, the determination of the individual contribution of these multiple interface interactions cannot be performed experimentally. Therefore, understanding the relationship between the surface structure of idealized C–S–H interfacing with graphene and the mechanical properties of the reinforced system is key to being able to realize new C–S–H nanocomposites and enhance the mechanical properties of cement-based materials.

MD simulations were used in this study to investigate the tensile and shear properties of tobermorite 14 Å (T_{14})-based models for C–S–H reinforced with a single graphene sheet (GS). T_{14} has been shown to present structural similarity with C–S–H phases that have low Ca/Si ratios (less than 1) [2]. While other C–S–H phase models with variable Ca/Si ratios have been recently proposed as more realistic models [12,21,22], the goal here was to understand the effect of different, well-characterized and defectless interface structures on the mechanical properties of GS reinforced C–S–H nanocomposites. T_{14} is a layered structure that consists of calcium polyhedral layers with infinite silicate chains of the wollastonite-type that are connected on both sides. The layered structure of T_{14} allowed for the study of three well-defined structures with different, well-defined surfaces that could interface with the GS, resulting in three chemically different C–S–H–graphene interfaces: the surface water–GS interface, the octahedral calcium layer–GS interface, and the tetrahedral silicate layer–GS interface. Additionally, T_{14} allowed for understanding the mechanical response of the nanocomposite under the most pristine conditions (i.e., silicate chains with no defects). Compared to C–S–H with defective calcium silicate chains, the infinite connectivity of the silicate chains in the T_{14} structure has been shown to be responsible for a large plastic response in the post failure stage [10,23]. The defectless T_{14}–GS interfaces thus provided a blueprint for understanding the strengthening mechanisms of graphene along the basal planes of the C–S–H and the influence of the surface structure of C–S–H interfacing with graphene on the mechanical properties. It should, however, be noted that the C–S–H phase exists in the form of nanocrystallites (~5 nm in size) and that, in any real situation, the mechanical properties of carbon-reinforced cements would be controlled not only by the graphene interactions with the planar basal surfaces, but also with various other faces of the C–S–H nanocrystallites, including their edges. Stress–strain responses, strain energy densities, elastic and shear moduli, bulk moduli, and the direction dependence of the elastic modulus and linear compressibility were determined for the pristine T_{14} and GS reinforced T_{14} systems. The results revealed a greater in-plane strengthening effect of the GS when interfacing with water than with either of the solid surfaces (i.e., calcium or silicate surfaces), which was ascribed to the enhanced molecular friction caused by intermolecular forces with water between the GS and the T_{14} structure. This work provides new insights into the mechanism of nanoscale mechanical reinforcement of graphene cement composites and other graphene reinforced matrix composites.

2. Computational details

2.1. Simulation models and computational cells

Three T_{14}-based C–S–H models and three nanocomposites of T_{14} reinforced with GS were constructed from the primary skeleton of the T_{14} structure. The T_{14} structure contained octahedral calcium layers sandwiched between tetrahedral chains and surface and interlayer water (Fig. 1) and provided for three possible tobermorite–graphene interface structures along the basal plane in which the GS was interfaced with the surface water, the octahedral calcium layer, and the tetrahedral silicate layer.

2.1.1. Graphene sheet (GS)

The GS was modeled using the Visual Molecular Dynamics (VMD) software package [24]. The zigzag (ZZ) and armchair (AC) edges of the GS were oriented along the Cartesian coordinate axes X [1 0 0] and Y [0 1 0] directions, respectively (Fig. 2a). The GS was 22 Å × 28 Å in size and consisted of 252 sp^2 hybridized carbon (C) atoms in a hexagonal ring pattern. The C–C bond distances and ∠C–C–C angles were 1.418 Å and 120°, respectively. The thickness of the GS was 3.35 Å.

2.1.2. Tobermorite 14 Å-based models for C–S–H

The monoclinic T_{14} structure described by Bonaccorsi et al. [25] was used as the initial model to create T_{14}-based structures with three types of exposed surfaces (i.e, water, octahedral calcium, and tetrahedral silicate chains) to interface with the GS. The unit cell of T_{14} was built using MOLTEMPLATE software [26]. The T_{14} unit cell consisted of 124 atoms per unit cell with space group symmetry of B11*b* and had a calcium to silicon (Ca/Si) ratio of 0.833 and lattice parameters a = 6.735 Å, b = 7.425 Å, c = 27.987 Å, $\alpha = \beta = 90°$, and $\gamma = 123.25°$. An occupancy factor of 1.0 was used in this work for the water molecules, resulting in a water to silicon ratio of 1.66. A full site occupancy was chosen to study the effect of the extreme case of water occupancy in the T_{14} structure on the reinforcing effect of graphene. The tensile strength of graphene oxide reinforced C–S–H composites has been shown in the literature to be influenced by the presence of water [18].

The T_{14} structure with the exposed water layer surface ($T_{14}^{O_w}$ structure) was created by replicating the T_{14} unit cell in the X-, Y-, and Z-directions 4 × 4 × 1 times to form the $T_{14}^{O_w}$ supercell (Fig. 2b). The T_{14} structure with the exposed octahedral calcium surface ($T_{14}^{Ca_o}$ structure) was created by deleting the topmost water layer and silicate chains of the original T_{14} unit cell. To uphold the periodicity of the T_{14} unit cell, the resulting unit cell was mirrored along the negative Z-direction to account for the removal of the layer from the top, resulting in a unit cell with a water to silicon ratio of 1.58. The resulting unit cell was then replicated along the X-, Y-, and Z-directions 4 × 4 × 1 times to form the $T_{14}^{Ca_o}$ supercell. The T_{14} structure with the exposed tetrahedral silicate surface ($T_{14}^{Si_t}$ structure) was created by stripping off the topmost layer of water molecules from the original T_{14} unit cell, resulting in a water to silicon ratio of 1.5. The resulting unit cell was then replicated 4 × 4 × 1 times to form the $T_{14}^{Si_t}$ supercell. The simulation boxes of all T_{14}-based systems were then changed from monoclinic to *P*1 triclinic symmetry before being interfaced with the GS to allow for the box dimensions to change during the MD simulations. The lattice parameters of the systems became parallel to the triclinic box dimensions after invoking periodicity, resulting in T_{14}-based models with dimensions of 26.94 Å × 27.50 Å along the X- and Y-directions and 29.53 Å, 27.77 Å, 28.05 Å along the Z-direction for $T_{14}^{O_w}$, $T_{14}^{Ca_o}$, and $T_{14}^{Si_t}$, respectively.

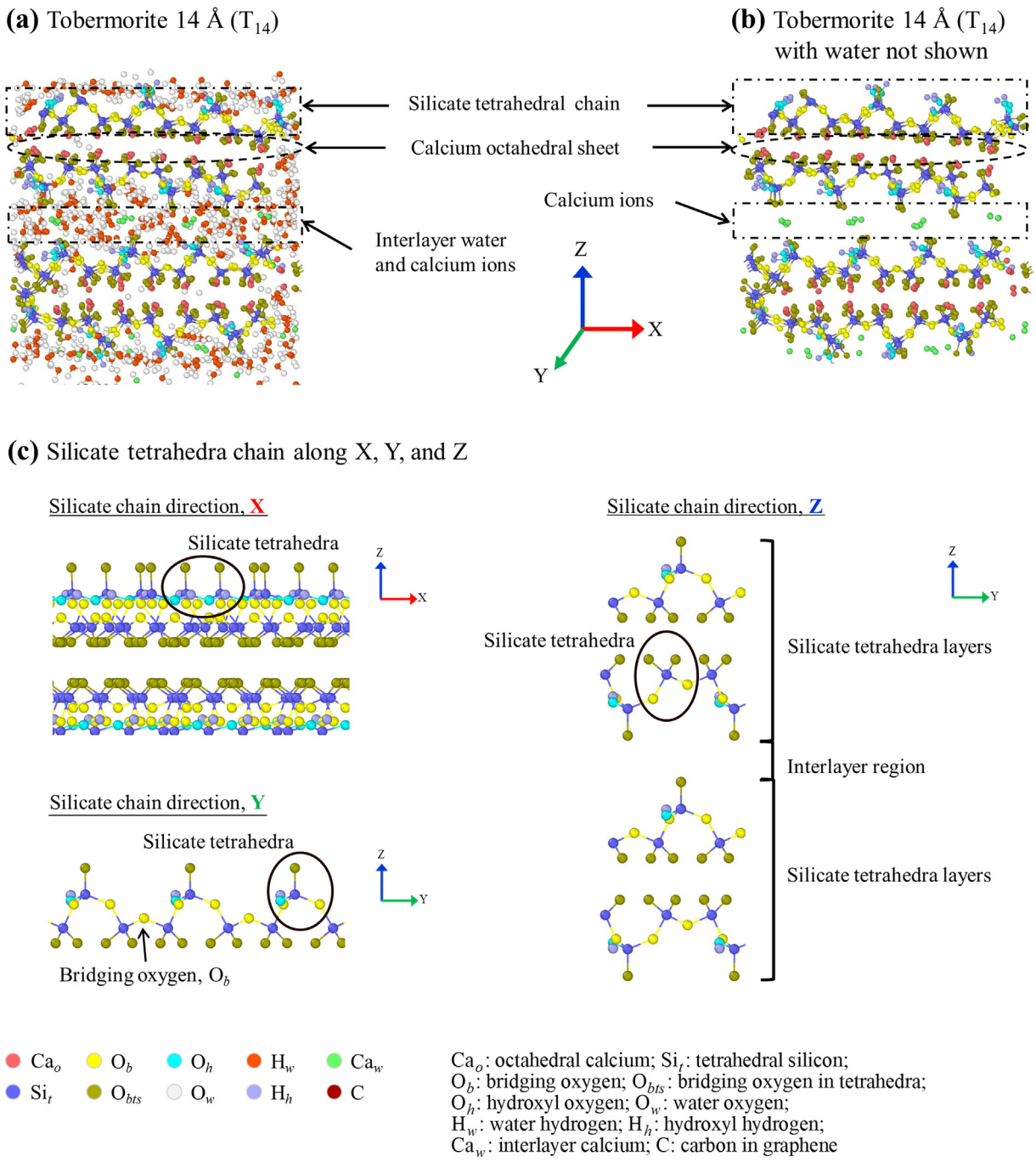

Fig. 1. (a) and (b) Layered crystal structure of tobermorite 14 Å (T_{14}). (c) Silicate tetrahedra chain along the X-, Y-, and Z-directions. [For clarity, structures are shown without water molecules in (b) and (c)].

2.1.3. T_{14}/GS nanocomposite models

To create the different T_{14}/GS nanocomposites, the triclinic T_{14}-based structures were interfaced with the GS. The nanocomposite with the GS interfacing with the surface water ($T_{14}^{O_w}$/GS nanocomposite; Fig. 3a) was constructed by placing the GS at a distance of 4 Å below the $(0\ 0\ \bar{1})$ plane of the $T_{14}^{O_w}$ supercell with the ZZ edge of the GS oriented along the X-axis and the AC edge oriented along the Y-axis. Similarly, the nanocomposite with the GS interfacing with the octahedral calcium layer at the (0 0 1) plane ($T_{14}^{Ca_o}$/GS nanocomposite; Fig. 3b) and the nanocomposite with the GS interfacing with the tetrahedral silicate layer at the (0 0 1) plane ($T_{14}^{Si_t}$/GS nanocomposite; Fig. 3c) were constructed by placing the GS at a distance of 5 Å above the exposed octahedral calcium surface of the $T_{14}^{Ca_o}$ supercell and the tetrahedral silicate surface of the $T_{14}^{Si_t}$ supercell, respectively, with the ZZ edge of the GS oriented along the X-axis and the AC edge oriented along the Y-axis. The resulting computational cells had dimensions of 26.94 Å × 27.50 Å × 35 Å and contained a total of 2236 atoms for the $T_{14}^{O_w}$/GS nanocomposite, 1856 atoms for the $T_{14}^{Ca_o}$/GS nanocomposite, and 1904 atoms for the $T_{14}^{Si_t}$/GS nanocomposite.

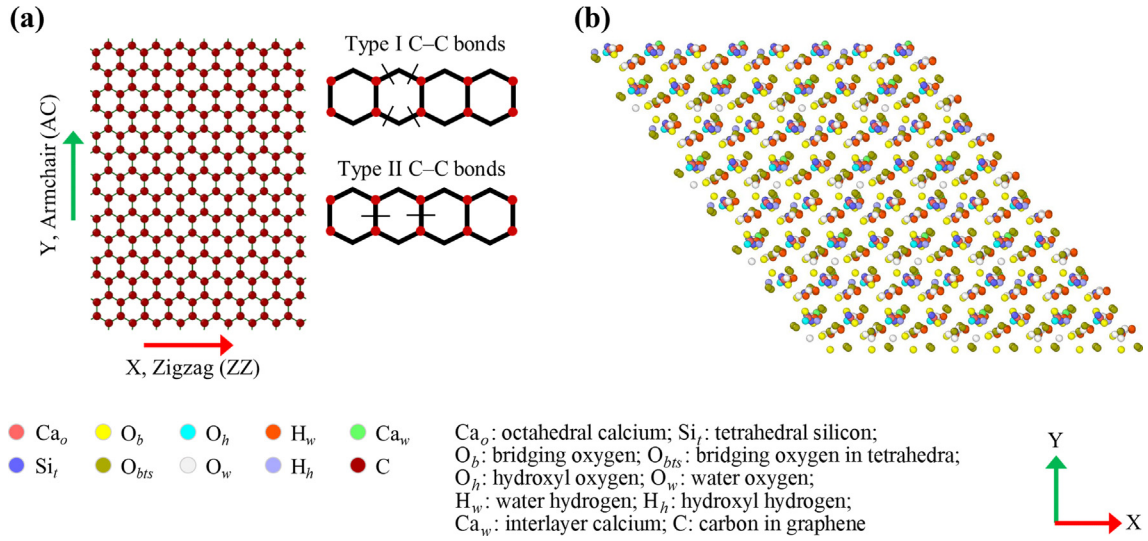

Fig. 2. (a) Graphene sheet (GS) and (b) monoclinic supercell of tobermorite 14 Å with the exposed water layer surface ($T_{14}^{O_w}$ supercell).

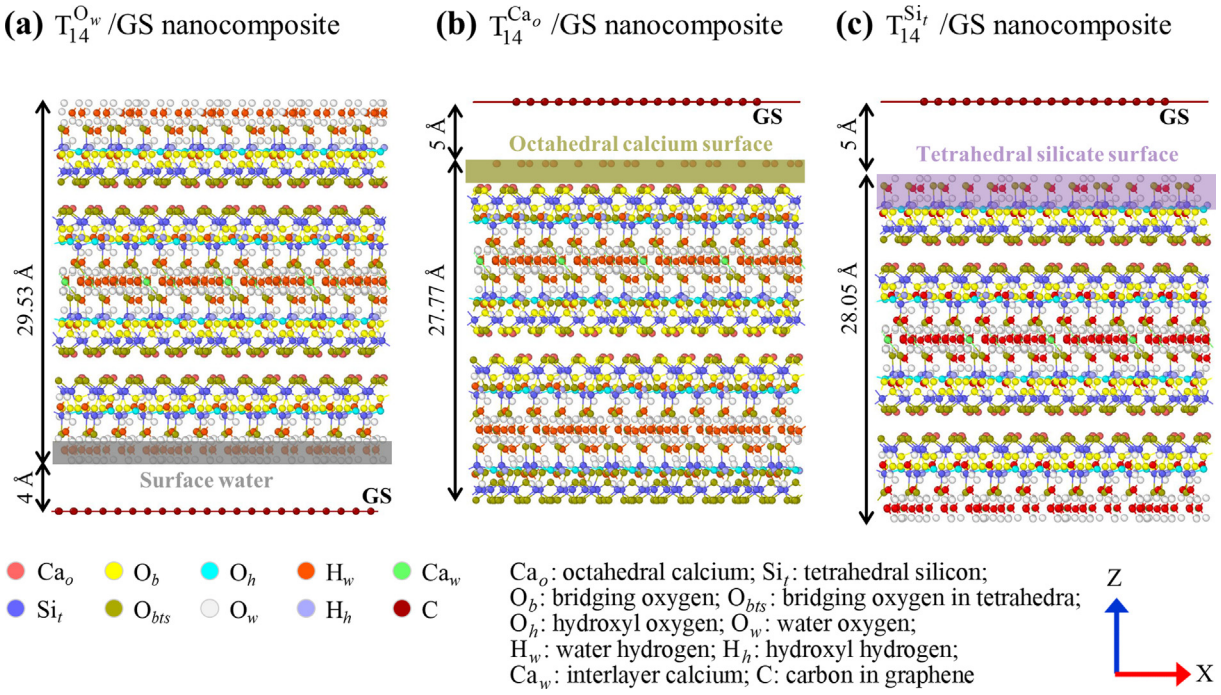

Fig. 3. Models of T_{14}/GS nanocomposites: (a) nanocomposite with the GS interfacing with the bottom surface water at the (0 0 $\bar{1}$) plane of the T_{14} structure ($T_{14}^{O_w}$/GS nanocomposite), (b) nanocomposite with the GS interfacing with the octahedral calcium layer at the (0 0 1) plane ($T_{14}^{Ca_o}$/GS nanocomposite), and (c) nanocomposite with the GS interfacing with the tetrahedral silicate layer at the (0 0 1) plane ($T_{14}^{Si_t}$/GS nanocomposite).

2.2. Force field

The Consistent Valence Force Field (CVFF) was employed for the simulation of the GS [27]. The CVFF has been previously shown to properly represent the tensile and shear properties of graphene and carbon nanotubes [18,28,29] and has been used in the study of the interactions of graphitic structures with tobermorite and aqueous solutions [30,31]. The C–C bond interaction of the GS was simulated with the Morse potential [32]. The angle bending, torsion, and improper interactions were simulated using the harmonic parameters of the CVFF. The partial atomic charges, non-bonded and bonded interactions among the T_{14} atoms were simulated using the Clay force field (ClayFF) [33,34], which relied on the flexibility of coulombic interactions between the interacting atoms to represent bonding. The ClayFF was developed to study the structural and dynamic properties of hydrated and mineral systems [33–37] and has been successfully used to study the mechanical and elastic properties of clay-based minerals and clay-based nanocomposites [37–41]. While using the ClayFF has been reported to generally reproduce well the out-of-plane elastic constants and overpredict the in-plane elastic properties of cement-related phases [37,38,42–44], in this study, the response of the GS was dominant in the T_{14}/GS nanocomposite systems and an overprediction of the elastic properties of the T_{14} systems was thus considered to have a minimal effect on the elastic properties of the overall nanocomposites. In addition, while ClayFF cannot capture

chemical reactions, hydrolytic reactions during loading of the T_{14}/GS systems (i.e., formation of silanol, Si–O–H groups and calcium hydroxyl, Ca–O–H groups as Si–O–Si or Si–O–Ca bonds break during loading) were considered to play a minimal role as it has been reported in the literature that water dissociation in graphene oxide reinforced C–S–H with low Ca/Si ratios (less than 1) was minimal for strain less than 0.4 [14] as was the case in this study. The interactions among the carbon atoms of the GS and T_{14} atoms were modeled using the Lennard-Jones (LJ) potential [45]. The values of the CVFF and ClayFF parameters are provided in the Supplementary material, Section S1.0.

2.3. Equilibration

All MD simulations were performed using LAMMPS, an open-source MD simulation software [46]. The pristine T_{14} systems (i.e., $T_{14}^{O_w}$, $T_{14}^{Ca_o}$, and $T_{14}^{Si_t}$) and the T_{14}/GS nanocomposites (i.e., $T_{14}^{O_w}$/GS, $T_{14}^{Ca_o}$/GS, and $T_{14}^{Si_t}$/GS) were energy minimized at 0 K using the conjugate gradient method to reduce the excess pressure build-up during the geometry setup. The pristine T_{14} systems and T_{14}/GS nanocomposites were then equilibrated for 1 ns and 500 ps, respectively, at 300 K and 0 atm, using NPT (fixed number of atoms, pressure, and temperature) ensemble conditions. The Nosé-Hoover thermostat and barostat were used for temperature and pressure control of the systems with 100 fs and 1000 fs damping constants, respectively [47,48]. The neighbor cut-off distance for the interacting atoms was 5 Å, and the neighbor list was updated every timestep. The long-range coulombic interactions were computed in the reciprocal space by the Particle-Particle-Particle-Mesh (PPPM) solver. The short-range coulombic interactions between atoms were calculated as:

$$\Psi^{coul} = \frac{1}{4\pi\in_0}\cdot\frac{q_i q_j}{r_{ij}^2} \quad (1)$$

where q_i and q_j are charges on atoms i and j, $\in_0$ is the permittivity of the vacuum (8.85419×10^{-12} F/m) and $r_{ij}=|r_i-r_j|$ is the interatomic distance. The short-range van-der-Waals (vdW) interaction was computed by the Lennard-Jones (LJ) potential using:

$$\Psi^{LJ} = 4\in\left[\left(\frac{\sigma}{r}\right)^{12}-\left(\frac{\sigma}{r}\right)^{6}\right] \quad (2)$$

where $\in$ is the depth of the potential well (kcal mol^{-1}), σ is the distance (Å) at which the potential was zero, and r is the interatomic distance (Å). The Lennard-Jones (LJ) and coulombic cut-off distances were 12 Å and 10 Å, respectively. The interactions between unlike atoms were calculated using the *Lorentz-Berthelot* mixing rules [49,50]. The time integration was performed using the velocity-Verlet algorithm. All simulations were performed using a 1 fs timestep. Periodic boundary conditions in the X-, Y-, and Z-directions were used for all systems.

2.4. Loading methods and MD simulations

Three different loading modes were used: (i) in-plane uniaxial tension along the X- and Y-directions (ZZ edge and AC edge of the graphene sheet, respectively for the nanocomposites), (ii) out-of-plane uniaxial tension along the Z-direction, and (iii) shear loading in the XY plane (perpendicular to the interface with the GS for the nanocomposites) along the X-direction. To simulate the loading and ensure an equal deformation pathway and uniform stress distribution, atoms at opposite edges of the T_{14} systems or T_{14}/GS nanocomposites and within 3 Å from the edge were constrained while subjected to in-plane tensile (atoms along the direction of stretching) and shear forces (top and bottom atoms) and within 4 Å (top and bottom atoms) for out-of-plane (Z-direction) tensile loading. A strain rate of $1\times10^{-5}\,\frac{Å}{Å}fs^{-1}$ was used for all loading modes. This strain rate was within the typical ranges used in the literature [51–53]. While stretching in one direction, the pressure in the other two directions was kept at zero to allow for the Poisson's effect. The time integration of the systems was performed under the NPT conditions for tensile loading and NVT (fixed number of atoms, volume, and temperature) conditions for shear loading.

2.5. Data collection and analysis

The atomistic stress was calculated from the Virial stress theorem [54] considering both the potential and kinetic energy terms. The time-averaged engineering stress was output every 500 fs and plotted against the corresponding strain to obtain the stress–strain ($\sigma-\varepsilon$) curve of each system. The strain energy densities per unit volume for tensile (Γ) and shear (Π) were calculated by integrating with the trapezoidal rule to obtain the area under the corresponding stress–strain curve from a strain of 0.0 to the fracture strain. The strain energy density was used as an indirect indication of the fracture toughness of the systems.

The intrinsic (equilibrium, zero strain) elastic stiffness constants (C_{ij}) and effective (i.e., during the elastic loading stage) elastic stiffness constants (C_{ij}^{eff}) of the systems were computed in the isothermal-isobaric ensemble (NPT) for the normal constants (C_{ij} and C_{ij}^{eff}, where $i=j=1, 2, 3$) and the canonical ensemble (NVT) for the shear constants (C_{ij} and C_{ij}^{eff}, where $i=j=4, 5, 6$). The system under consideration was displaced from its equilibrium position at 0.0 strain (intrinsic elastic constants) or from its position at 0.025 strain (effective elastic constants) to a specified strain, ε_j ($j=X,Y$), and equilibrated for 5000 fs (long enough to reach stress convergence). The collected stress data, σ_i ($i=X,Y$), were then time-averaged to get one σ_i point. The method was repeated for five values of ε_j from −0.01 to + 0.01 with 0.005 strain increment (i.e., −0.01, −0.005, 0, 0.005 and 0.01) for the intrinsic constants and three values of ε_j from 0 to 0.05 with 0.025 strain increment (i.e., 0. 0.025, and 0.05) for the effective constants. The C_{ij} and C_{ij}^{eff} were then calculated from the slope of the $\sigma_i-\varepsilon_j$ plot. This method (known as the direct method [28,55–57]) was used to obtain all independent intrinsic (C_{ij}) and effective (C_{ij}^{eff}) constants of the elastic tensor for all systems. While the triclinic T_{14} systems have twenty one (21) independent C_{ij} and C_{ij}^{eff}, the normal-shear coupling elastic constants (C_{ij} and C_{ij}^{eff}, where $i\neq$ j, and $i=1, 2, 3$, $j=4, 5, 6$) were approximately zero compared to the normal and shear elastic stiffness constants. The orthorhombic symmetry with nine (9) elastic constants (including normal, shear, and normal coupling constants) was thus assumed for both the T_{14} systems and T_{14}/GS nanocomposites. The Born mechanical stability criteria were calculated to check for the mechanical stability of all systems [58,59]. The compliance tensor was calculated by inverting the stiffness matrix, $S\equiv C^{-1}$. The compliance tensor (S) was then used to calculate the elastic moduli (E), shear moduli (G), bulk moduli (κ), volume compressibility (β_v) and linear compressibility (β_L).

3. Results and discussion

3.1. Stress-strain response

3.1.1. In-plane uniaxial tensile loading

The GS significantly increased the in-plane (X- and Y-directions) fracture tensile strength and strain of the T_{14} systems (Fig. 4). For all T_{14}/GS nanocomposites, greater in-plane fracture tensile strength and strain were observed for loading in the X-direction compared to the Y-direction as a result of the orientation of the ZZ and AC edges (along X- and Y-directions, respectively) of the

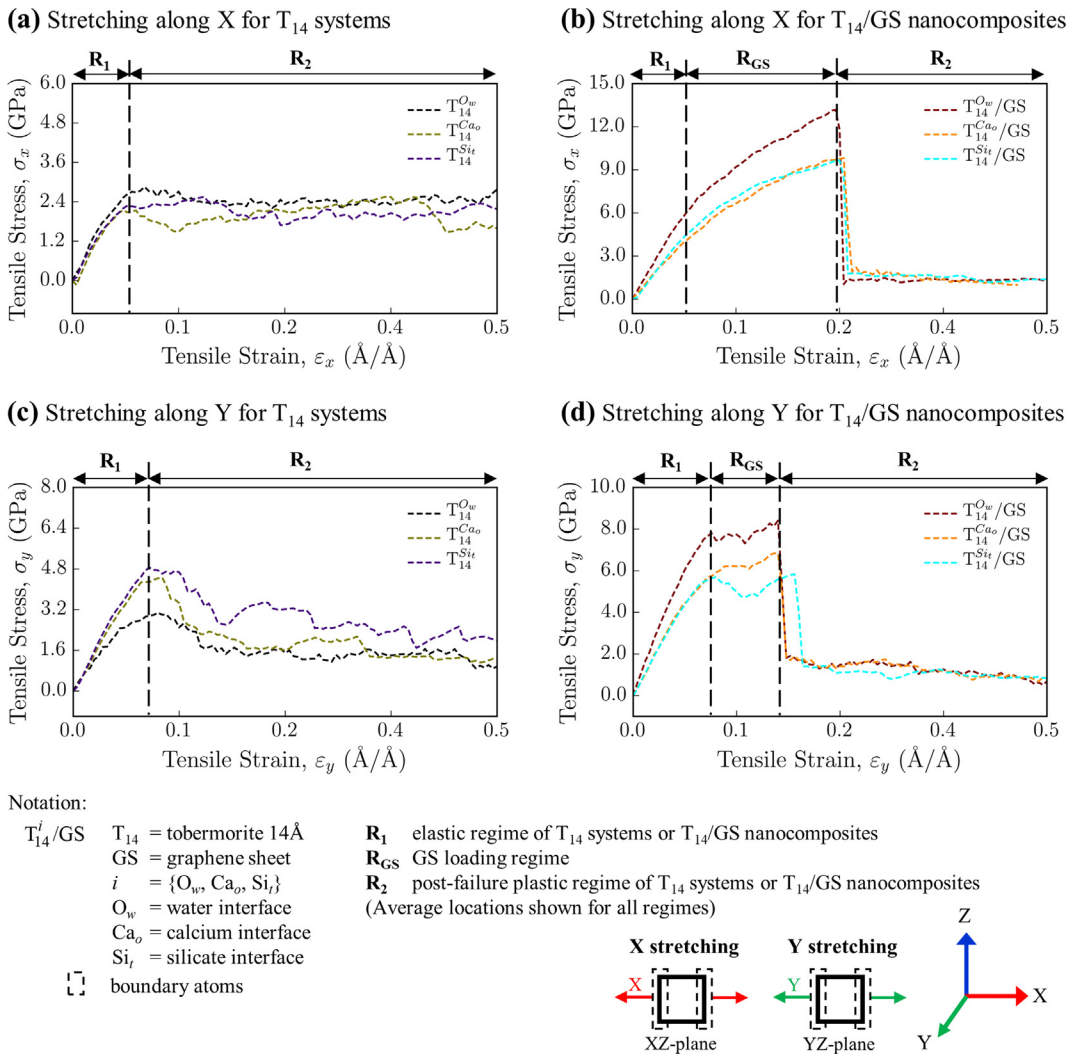

Fig. 4. Stress–strain response under in-plane tensile loading: (a) and (b) stretching along the X-direction of T_{14} systems and T_{14}/GS nanocomposites, respectively and (c) and (d) stretching along the Y-direction of T_{14} systems and T_{14}/GS nanocomposites, respectively. [$T_{14}^{O_w}$: T_{14} structure with exposed water layer surface; $T_{14}^{Ca_o}$: T_{14} structure with exposed octahedral calcium surface; $T_{14}^{Si_t}$: T_{14} structure with exposed tetrahedral silicate surface; $T_{14}^{O_w}$/GS: GS interfacing with the bottom surface water of T_{14}; $T_{14}^{Ca_o}$/GS: GS interfacing with the octahedral calcium layer of T_{14}; $T_{14}^{Si_t}$/GS: GS interfacing with the tetrahedral silicate layer of T_{14}].

GS in the T_{14}/GS nanocomposites. The GS is more stretchable in the ZZ direction, whereas it breaks earlier (lower strain and stress) when stressed in the AC direction because of the bonding arrangements of the hexagonal graphene lattice [28]. The GS increased the in-plane failure stress of the T_{14} systems by as much as 180% and 145% in the X- and Y-directions, respectively.

T_{14} systems. The in-plane results for the pristine T_{14} systems (Fig. 4a and c) showed overall good agreement with atomistic studies reported in the literature in the X- and Y-directions with a greater in-plane fracture tensile strength in the Y-direction than in the X-direction as a result of the silicate chain of the T_{14} systems running parallel to the Y-direction (greater linear density in that direction). The in-plane fracture tensile strength of the T_{14} systems was 2.8 GPa, 2.2 GPa, and 2.3 GPa for $T_{14}^{O_w}$, $T_{14}^{Ca_o}$, and $T_{14}^{Si_t}$, respectively, in the X-direction and 3.1 GPa, 4.5 GPa, and 4.9 GPa, respectively, in the Y-direction, which compared well with simulation values reported in the literature that ranged from 3 to 4.5 GPa [9,60]. The differences observed in the in-plane fracture tensile strength between the T_{14} systems were due to structural differences in their crystal structure assembly with respect to the position of the silicate tetrahedral layer, calcium octahedral layer, and interlayer water within the structure (different representative volume elements, RVE) and were consistent with the water to silicon ratio of the structures (greater ratio, i.e. more water molecules, for $T_{14}^{O_w}$, resulting in a lower tensile strength parallel to the silicate chain). The chemical composition of tobermorite and C–S–H structures has been shown experimentally to affect the atomic packing density of the structure [61]. In addition, the amount of water molecules in the C–S–H structure has been reported, using molecular modeling, to influence its tensile strength with a lower strength seen with increasing amount of water [62]. After fracture, all T_{14} systems exhibited a plastic regime that was attributed to a local structure rearrangement with internal displacements and rotations of the atoms in the silicate tetrahedral and calcium octahedral layers as a result of the infinite connectivity of the silicate chains, thus allowing the systems to continue to withstand strain. A similar plastic response in the post failure stage of in-plane tensile loading has been reported in the literature for tobermorite and C–S–H with low Ca/Si ratios (i.e., more polymerized and less defective silicate chains) [12,23].

T_{14}/GS nanocomposites. The in-plane tensile stress–strain response of the T_{14}/GS nanocomposites (Fig. 4b and d) was similar to that

observed in fiber–matrix composites with lamellar formation [63] and exhibited three main regimes: (i) an elastic regime in which the stress increased quasi-linearly with the strain as T_{14} and the GS shared the stress up to the failure of the T_{14} matrix (regime R_1); (ii) a regime in which the GS controlled the stress–strain evolution of the nanocomposite and was capable of bearing the increasing strain without any bond breaking (GS loading regime, $R_{GS;}$); and (iii) a post failure plastic regime (regime R_2). After failure of the T_{14} matrix and as the stress within the T_{14}/GS nanocomposites increased, internal displacements of the atoms in the silicate tetrahedral and calcium octahedral layers became more prominent, resulting in disordered layers. Meanwhile, the GS provided a crack bridging mechanism, thus allowing the nanocomposites to maintain overall structural integrity until fracture of the GS. Figs. 5 and 6 illustrate the failure stages of the $T_{14}^{O_w}$/GS nanocomposite during tensile loading along the X- and Y-directions, respectively, showing (i) displacement of atoms in the calcium octahedral and silicate tetrahedral layers, (ii) breaking of bonds between tetrahedral silicon and oxygen atoms (Si_t–O) and between interlayer calcium and bridging oxygen in tetrahedra (Ca_w–O_{bts}), and (iii) the crack path and separation of the structural layers. Similar failure stages were seen for the $T_{14}^{Ca_o}$/GS and $T_{14}^{Si_t}$/GS nanocomposites. At the fracture of the GS, the silicate tetrahedral and calcium octahedral layers were critically damaged and had then no capacity to support further loads. At that point, the T_{14}/GS nanocomposites failed abruptly and the stress then went to a plastic plateau. The strengthening effect of the GS, however, still existed even though the GS had ruptured. The T_{14}/GS nanocomposites showed fracture tensile strengths and strains that were as much as 360% and 260% in the X-direction and 180% and 110% in the Y-direction greater, respectively, than that of the T_{14} systems without the GS reinforcement.

The evolution of the Si_t–O and C–C bond lengths as a function of strain along the X- and Y-directions (Fig. 7, shown for the $T_{14}^{O_w}$/GS nanocomposite) further illustrated the strain transfer from the T_{14} structure to the GS with an initial rapid increase in the Si_t–O bond length followed by a gradual decrease that was accompanied by a sharp increase in the C–C bond length for stretching along the X-direction and to a lesser extent along the Y direction (only type II bonds were involved during stretching along X while two type I bonds participated during stretching along Y). It also further confirmed the role played by the Si_t–O bond stretching in the existence of residual stress in the post failure plastic regime. Analysis of the number of Si_t–O bonds broken (Fig. 8) revealed a lower number of broken bonds with increasing strain for the nanocomposite with the GS interfacing with the surface water ($T_{14}^{O_w}$/GS) compared to the nanocomposites with the GS interfacing with the calcium and silicate surfaces ($T_{14}^{Ca_o}$/GS and $T_{14}^{Si_t}$/GS). This lower number of broken Si_t–O bonds within the $T_{14}^{O_w}$/GS nanocomposite became apparent only after failure of the $T_{14}^{O_w}$ matrix when the GS took control of the stress–strain evolution and suggested a different flow of stress within this nanocomposite. A lower number of broken Si_t–O bonds was also observed for the pristine $T_{14}^{O_w}$ structure compared to the $T_{14}^{Ca_o}$ and $T_{14}^{Si_t}$ structures. The water layers within the $T_{14}^{O_w}$ structure were thought to have hindered the propagation of stress across the structure (three water layers within the RVE of the $T_{14}^{O_w}$ system versus two water layers within the RVE of the $T_{14}^{Ca_o}$ and $T_{14}^{Si_t}$ systems). Overall, a lower number of broken bonds was seen for loading in the Y-direction compared to loading in the X-direction because the stress during loading in the Y-direction was transferred through the bridging oxygen, which could twist and rotate upon loading, thus preventing bond breaking.

The GS exhibited more apparent in-plane strengthening effect when interfacing with water than with either of the solid surfaces (i.e., calcium or silicate surfaces). The $T_{14}^{O_w}$/GS nanocomposite with the GS interfacing with the bottom surface water (water interface) exhibited the highest fracture tensile strengths (13.2 GPa in the X-direction and 8.4 GPa in the Y-direction). In contrast, the $T_{14}^{Ca_o}$/GS nanocomposite with the GS interfacing with the octahedral calcium layer (calcium interface) and the $T_{14}^{Si_t}$/GS nanocomposite with the GS interfacing with the tetrahedral silicate layer (silicate interface) had lower in-plane fracture tensile strengths (9.8 GPa and 9.7 GPa, respectively, in the X-direction and 6.8 GPa and 5.8 GPa, respectively, in the Y-direction). The greater fracture strength seen with the water interface was attributed to the interaction of the water with the GS as confirmed by the local stress distribution at the GS surface. The GS interfacing with water demonstrated the highest local stress distribution compared to that of the GS interfacing with the calcium and silicate surfaces (Fig. 9). The water molecules at the surface of the T_{14} structure increased the intermolecular forces (i.e., molecular level frictional forces, the forces acting between the molecules of two different surfaces) with the GS most likely because of their preferential orientation in the confined space created by the interface with the GS, which has been reported in the literature to increase the water viscosity [64]. As a result, viscous interfacial water dominated and increased the surface friction, thus leading to a greater strength development of the overall nanocomposite than that seen when the GS interacted with the dry, solid surfaces (i.e., calcium and silicate surfaces) with no mediating water. By analogy, the behavior seen at the water–GS interface was similar to that occurring when water increases the friction between someone's finger and a sheet of plastic. Molecular level, water mediated friction versus dry friction at solid interfaces has been the focus of numerous studies [65–68] and enhanced friction forces with water have been reported at graphene/copper and graphene/mica interfaces [67,69].

The effect of the structure of the dry solid surface (calcium vs. silicate) interfacing with the GS was apparent only in the Y-direction (parallel to the silicate chain) with the lowest fracture strength obtained for the nanocomposite with the GS interfacing with the tetrahedral silicate layer. It was hypothesized that the structure of the octahedral calcium layer as an ordered zigzag sheet (corrugated surface) caused greater molecular friction with the GS than that of the tetrahedral silicate layer, which was more prone to twisting and rotating, thus resulting in a lower strength development for the nanocomposite with the silicate interface than that with the calcium interface. Overall greater local stresses at the GS surface were observed for the calcium interface compared to the silicate interface (Fig. 9).

3.1.2. Out-of-plane tensile loading

The in-plane GS reinforcement of the T_{14} structures did not show a strengthening of the structures along their weakest direction, i.e. the direction orthogonal to the interlayer water region (Z-direction). On the contrary, the presence of the GS along the basal plane caused a loss (as much as 47% reduction) in the out-of-plane tensile strength capacity of the T_{14} structures (Fig. 10).

T_{14} systems. The out-of-plane fracture tensile strength of the T_{14} structures in the Z-direction was controlled by the weak mechanical strength of the interlayer water region and was influenced by the relative position of the different layers through which the stress was transferred (Fig. 11). The fracture and separation of the structures occurred at the interlayer water region from the breaking of the bonds connecting the calcium-silicate layers (i.e., bonds between bridging oxygen from the silicate chains and the

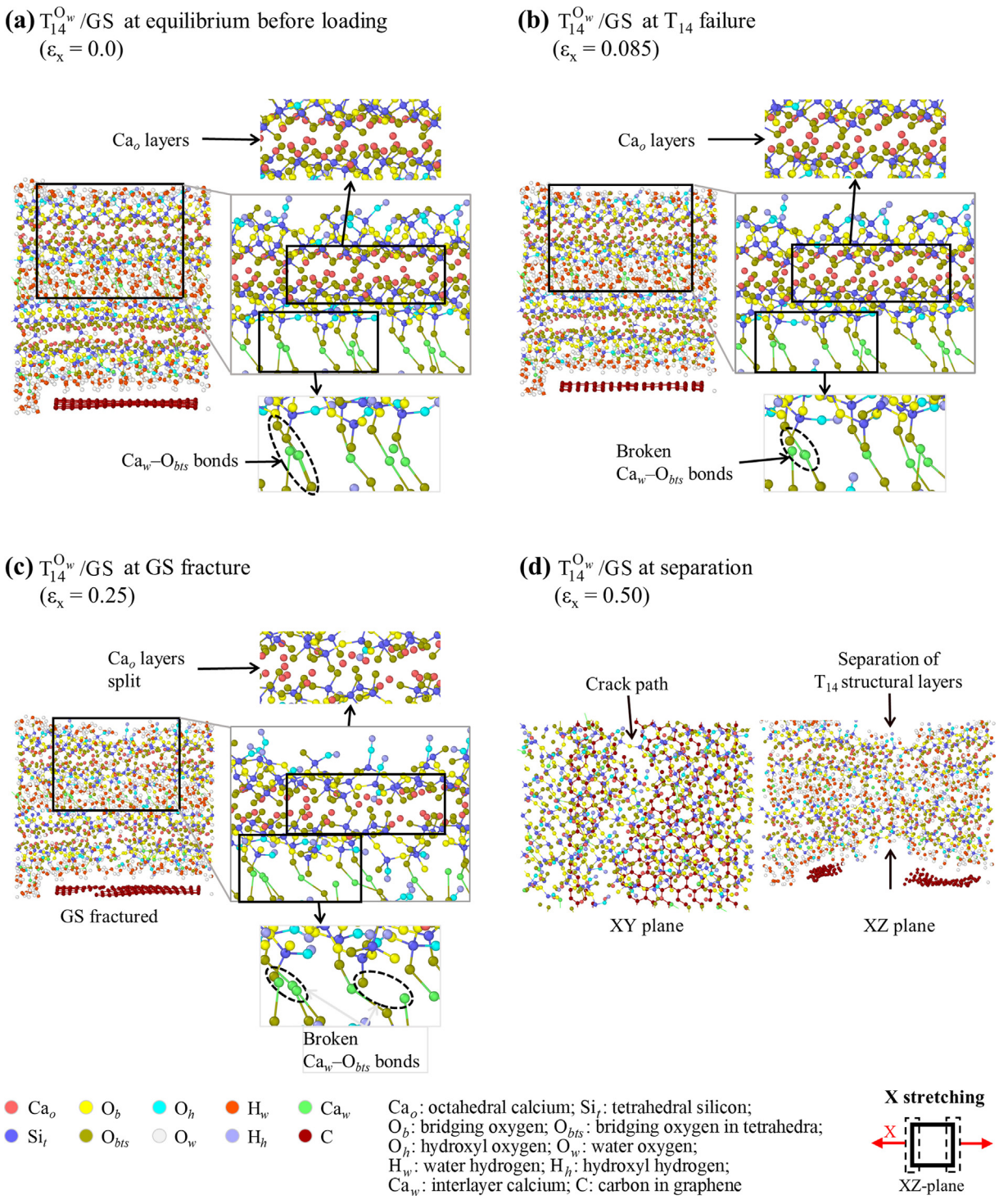

Fig. 5. Failure stages of the nanocomposite with the GS interfacing with the bottom surface water of the tobermorite 14 Å ($T_{14}^{O_w}$/GS nanocomposite) during in-plane tensile loading along the X-direction: (a) after relaxation to equilibrium but before tensile loading (unstrained conditions); (b) at failure of the tobermorite 14 Å (T_{14}) matrix; (c) at fracture of the graphene sheet (GS); and (d) after separation of the structural layers. [For clarity, structures in insets are shown without water molecules].

interlayer calcium atoms, O_{bts}–Ca_w–O_{bts} bridging bonds). The T_{14} structure with the exposed octahedral calcium surface ($T_{14}^{Ca_o}$ structure) showed the highest out-of-plane fracture tensile strength (1.7 GPa) in the Z-direction (Fig. 10a) while that with the exposed water layer surface ($T_{14}^{O_w}$ structure) had the lowest (1.1 GPa). The innermost layer of the $T_{14}^{Ca_o}$ structure was composed of calcium octahedral sandwiched by silicate tetrahedral chains thus providing the $T_{14}^{Ca_o}$ structure with greater stress resistance (greater capability to take up load) in the Z-direction than the two other T_{14} structures ($T_{14}^{O_w}$ and $T_{14}^{Si_t}$) for which the innermost layer was composed of the weak interlayer water region. For all structures, during the separation process, the water molecules clustered within the interlayer water region and formed a water molecule chain connected by a dynamic hydrogen bond network (Fig. 11). Both ends of this chain were attached to the interlayer calcium atoms or bridging oxygen from the silicate chains, resulting in residual

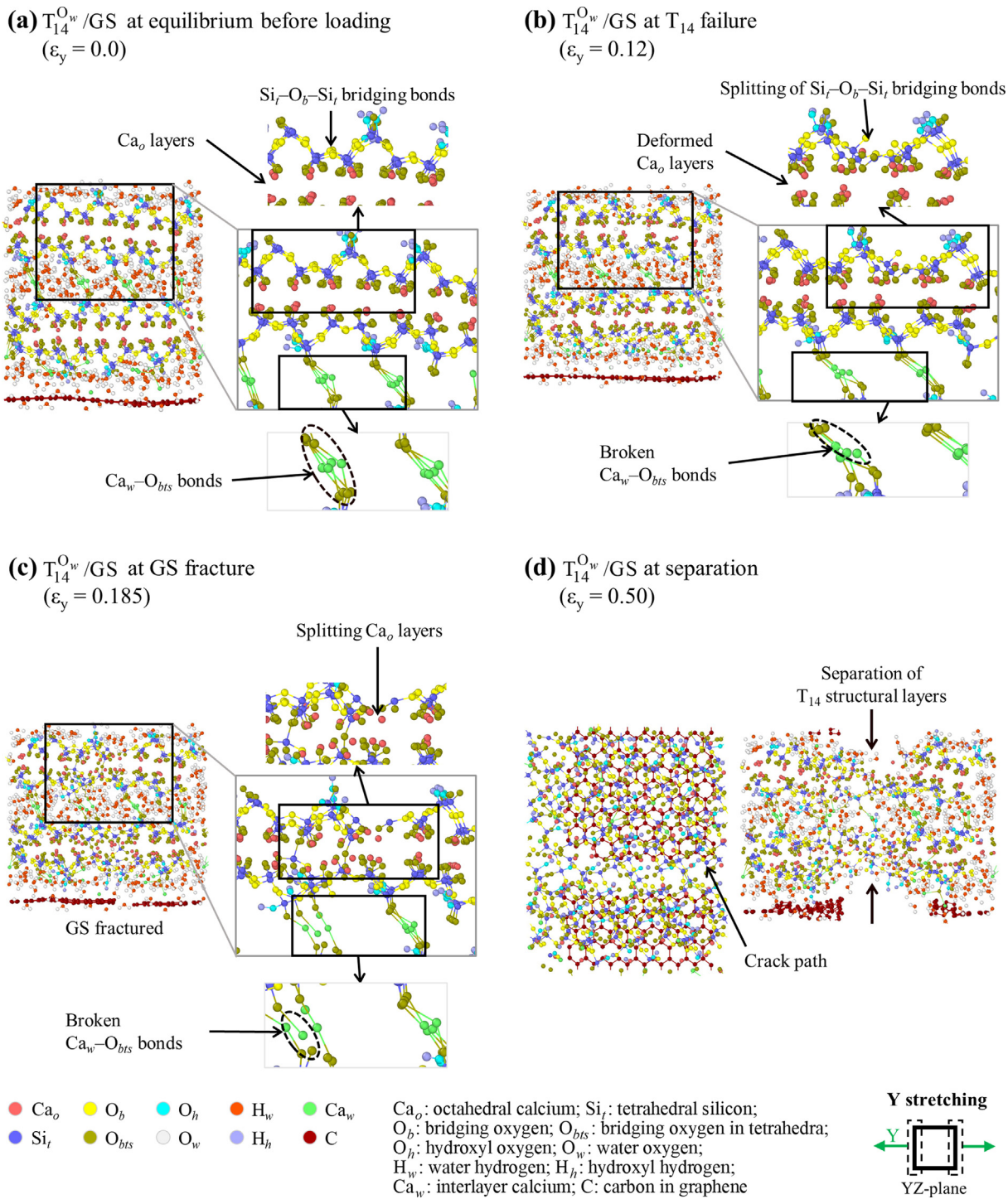

Fig. 6. Failure stages of the nanocomposite with the GS interfacing with the bottom surface water of the tobermorite 14 Å ($T_{14}^{O_w}$/GS nanocomposite) during in-plane tensile loading along the Y-direction: (a) after relaxation to equilibrium but before tensile loading (unstrained conditions); (b) at failure of the tobermorite 14 Å (T_{14}) matrix; (c) at fracture of the graphene sheet (GS); and (d) after separation of the structural layers. [For clarity, structures in insets are shown without water molecules].

stress characterized by a continued increase in strain capacity with a flattening of the stress retained.

T_{14}/GS nanocomposites. The presence of the GS as in-plane reinforcement had no strengthening effect on the T_{14} structures in the Z-direction (out-of-plane) and, on the contrary, degraded their out-of-plane tensile performance. The failure mode of the T_{14}/GS nanocomposites under tensile loading in the Z-direction differed significantly from that of the in-plane loading. The failure mode of the nanocomposites with the GS interfacing with the surface water and tetrahedral silicate layer (i.e., $T_{14}^{O_w}$/GS and $T_{14}^{Si_t}$/GS) was dominated by the failure of the interface between the T_{14} structure and the GS while that of the nanocomposite with the GS interfacing with the octahedral calcium layer (i.e., $T_{14}^{Ca_o}$/GS) was controlled by a failure within the T_{14} structure. For the $T_{14}^{O_w}$/GS and $T_{14}^{Si_t}$/GS nanocomposites, the separation of the GS and T_{14} structure as a result of the pulling in the Z-direction occurred at the interface

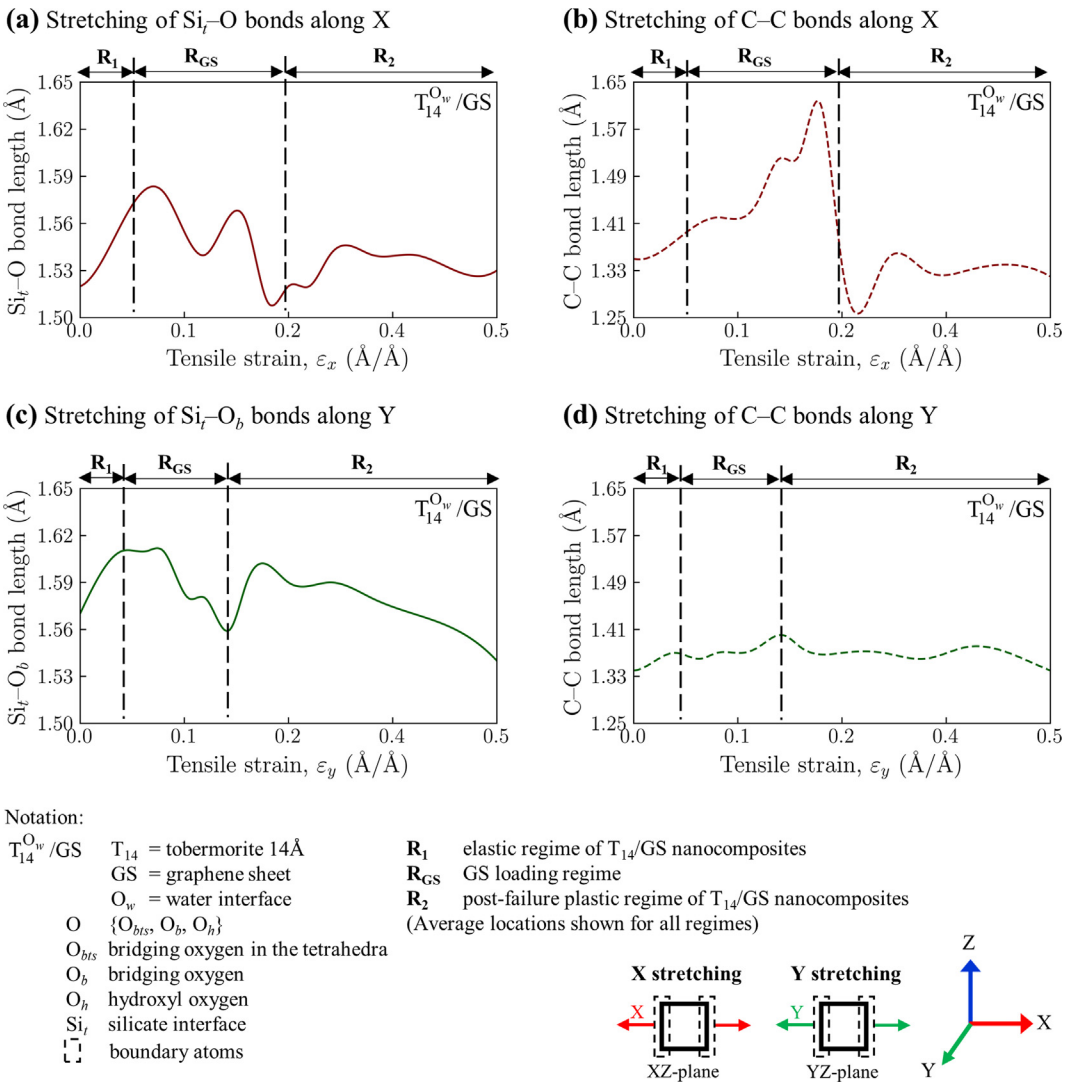

Fig. 7. Evolution of tetrahedral silica–oxygen bond length and carbon–carbon bond length during in-plane tensile loading of the nanocomposite with the GS interfacing with the bottom surface water of the tobermorite 14 Å ($T_{14}^{O_w}$/GS nanocomposite): (a), (b) Si$_t$–O bond length and C–C bond length, respectively during stretching along the X-direction and (c), (d) Si$_t$–O$_b$ bond length and C–C bond length, respectively during stretching along the Y-direction.

with the GS rather than inside the bulk of the T_{14} structure and no local separation within the T_{14} structure occurred (Fig. 11d and f). The clean separation suggested that the surface water–GS interface and tetrahedral silicate layer–GS interface were mechanically weaker than the GS or the T_{14} structures. In contrast, for the $T_{14}^{Ca_o}$/GS nanocomposite, the separation occurred inside the bulk of the T_{14} structure with fracture of the interlayer water region similar to that of the pristine system with no GS reinforcement (Fig. 11e). In all cases, the T_{14} structures became elongated as the interatomic bonds were stretched, and some structural water molecules were seen to have migrated towards the interface with the GS. At the peak stress, the T_{14} structures were lengthened in the Z-direction by *ca.* 6% for the $T_{14}^{O_w}$/GS nanocomposite, *ca.* 9% for the $T_{14}^{Ca_o}$/GS nanocomposite, and *ca.* 2.4% for the $T_{14}^{Si_t}$/GS nanocomposite. The greater elongation at peak stress seen for the $T_{14}^{Ca_o}$/GS nanocomposite indicated a greater resistance of this nanocomposite to tensile loading in the Z-direction. An analysis of the number of broken interlayer calcium–bridging oxygen in tetrahedra (Ca_w–O_{bts}) bonds indicated that the T_{14}/GS nanocomposites with the GS interfacing with the water and silicate surfaces had fewer Ca_w–O_{bts} bonds broken than the pristine T_{14} systems as strain progressed (Fig. 12), while that with the GS interfacing with the calcium surface demonstrated a similar number of broken Ca_w–O_{bts} bonds compared to its pristine counterpart (without GS reinforcement). The evolution of the number of broken Ca_w–O_{bts} bonds was consistent with the fact that the separation of the $T_{14}^{Ca_o}$/GS nanocomposite occurred at the interlayer water region versus at the interface between the GS and the T_{14} structure for the $T_{14}^{O_w}$/GS and $T_{14}^{Si_t}$/GS nanocomposites.

The out-of-plane stress–strain evolution exhibited three main regimes for all cases (Fig. 10b): (i) a strain hardening regime (R_h) in which the GS and the T_{14} structure pulled on each other and the nanocomposites started to elongate; (ii) a strain softening regime (R_s) in which the stress was relaxed with increasing strain as the nanocomposite separated at the fracture region; and (iii) a separation regime (R_{sep}) characterized by the presence of residual stresses. The nanocomposite with the GS interfacing with the octahedral calcium layer ($T_{14}^{Ca_o}$/GS) had a higher peak tensile separation stress than the two other T_{14}/GS nanocomposites (1.00 GPa versus 0.81 GPa and 0.78 GPa, for the nanocomposites with the GS interfacing with the water and silicate surfaces, respectively) and also showed a greater fracture strain

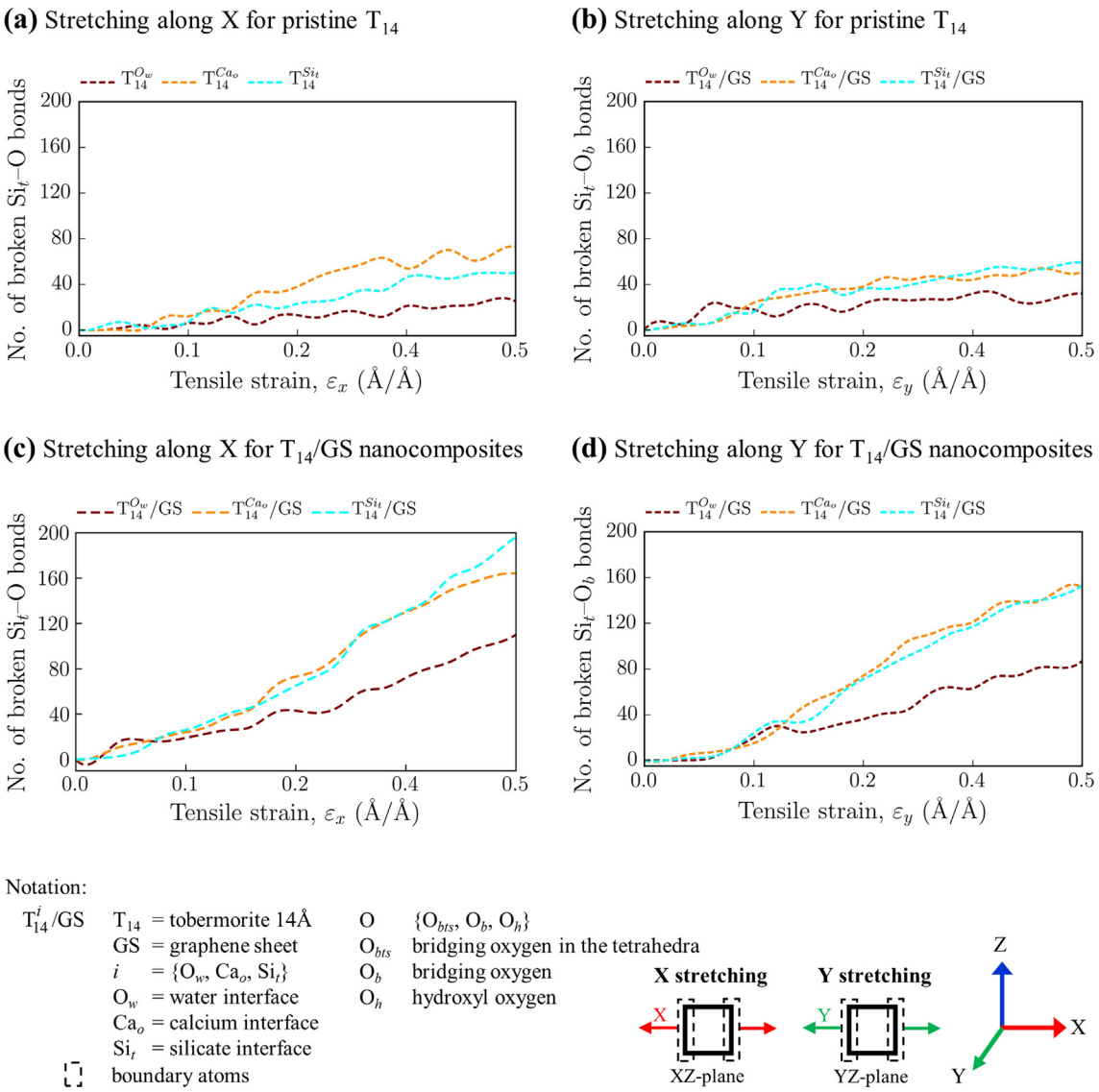

Fig. 8. Evolution of the number of broken tetrahedral silicon–oxygen bonds in the pristine T_{14} systems and T_{14}/GS nanocomposites as function of applied strain: (a), (b) during stretching of the pristine T_{14} systems along the X- and Y-directions, respectively and (c), (d) during stretching of the T_{14}/GS nanocomposites along the X- and Y-directions. [$T_{14}^{O_w}$: T_{14} structure with exposed water layer surface; $T_{14}^{Ca_o}$: T_{14} structure with exposed octahedral calcium surface; $T_{14}^{Si_t}$: T_{14} structure with exposed tetrahedral silicate surface; $T_{14}^{O_w}$/GS: GS interfacing with the bottom surface water of T_{14}; $T_{14}^{Ca_o}$/GS: GS interfacing with the octahedral calcium layer of T_{14}; $T_{14}^{Si_t}$/GS: GS interfacing with the tetrahedral silicate layer of T_{14}].

(0.11 versus 0.055 for both the $T_{14}^{O_w}$GS and $T_{14}^{Si_t}$/GS nanocomposites). This indicated that the $T_{14}^{Ca_o}$/GS nanocomposite needed more energy to fracture, due to a greater resistance to stress transfer in the Z-direction for the T_{14} structure with the exposed octahedral calcium surface ($T_{14}^{Ca_o}$ structure) compared to the other T_{14} structures, thus lowering the stress concentration at the interface with the GS and increasing the stress concentration within the interlayer water region. In contrast, the T_{14}/GS nanocomposites with the GS interfacing with the water and silicate surfaces showed similar stress development with increasing separation due to the similar organization within the structure of the different layers through which the stress was transferred. For the $T_{14}^{O_w}$/GS and $T_{14}^{Si_t}$/GS nanocomposites, after separation of the GS and T_{14} structures, a small residual stress could be seen as a result of the migration of the water molecules out of the T_{14} structures, forming collective hydrogen bond networks (i.e., T_{14}–water–water–[...]–water hydrogen bonds such as in Fig. 11) that interacted with the GS through repulsive van der Waals forces. For the $T_{14}^{Ca_o}$/GS nanocomposite, no more residual stress could be seen beyond a strain of 0.2.

3.1.3. Shear loading in the XY plane along the X-direction

Only shear loading along the X-direction (i.e., zigzag direction of the GS and the direction perpendicular to that of the running silicate chains) was examined because it was the T_{14} structures' weakest direction and the GS's more stretchable direction.

The GS significantly contributed to the fracture shear strength of the T_{14}/GS nanocomposites (Fig. 13). The T_{14}/GS nanocomposites exhibited fracture shear strengths that were 90% to 225% greater than that of their respective, pristine T_{14} systems without the GS reinforcement. The greatest enhancement of the fracture shear strength was seen for the $T_{14}^{O_w}$/GS nanocomposite with the GS interfacing with water while the smallest shear strength development was seen for the $T_{14}^{Si_t}$/GS nanocomposite.

The response of the T_{14}/GS nanocomposites to shear loading in the XY plane was influenced by the molecular friction forces

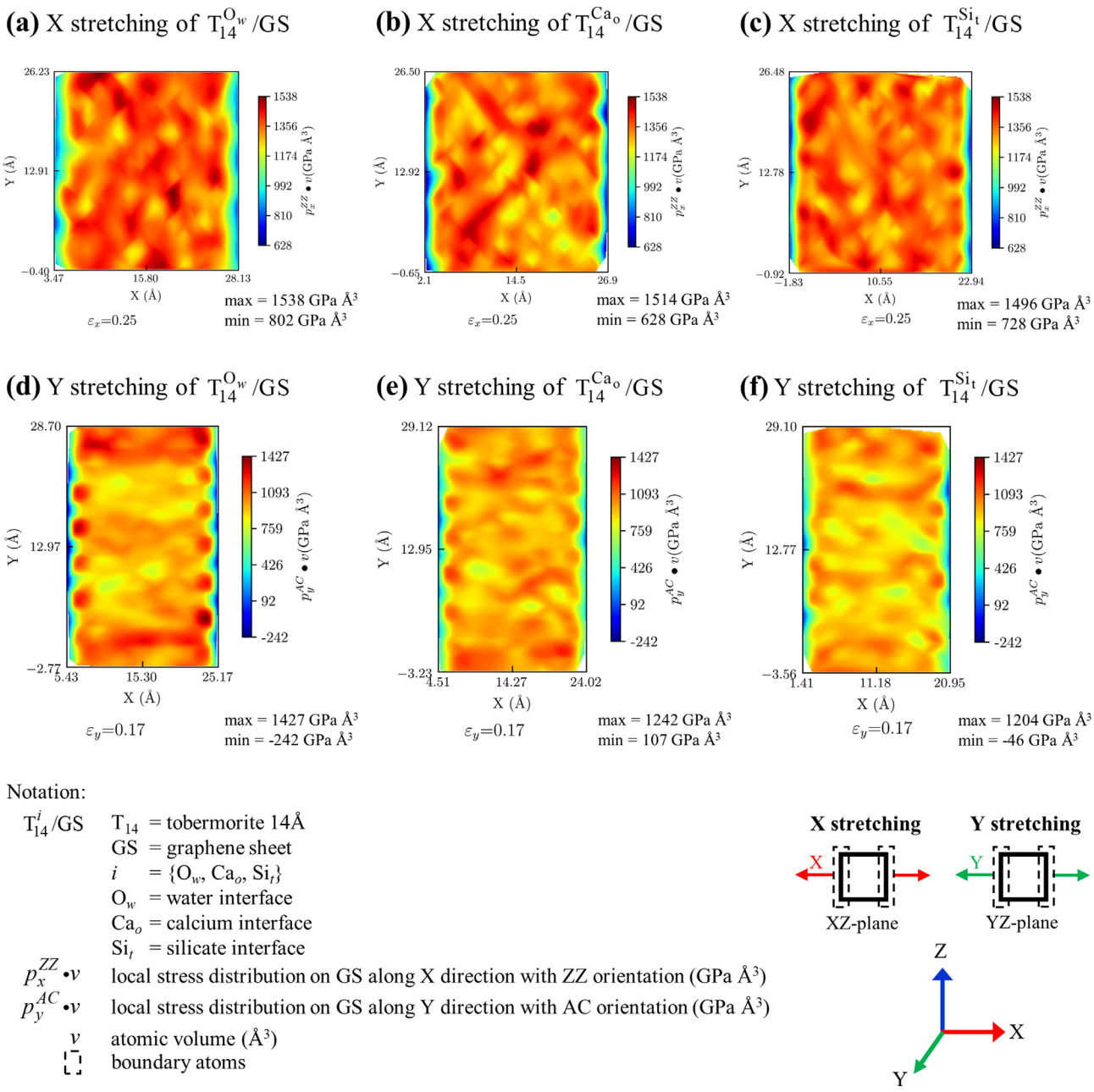

Fig. 9. Local stress distribution at the graphene sheet (GS) surface before fracture of the GS during tensile loading: (a), (b), and (c) X-direction stretching of the GS reinforced tobermorite 14 Å nanocomposites; and (e), (f), and (g) Y-direction stretching of the GS reinforced tobermorite 14 Å nanocomposites. [$T_{14}^{O_w}$/GS: GS interfacing with the bottom surface water of T_{14}; $T_{14}^{Ca_o}$/GS: GS interfacing with the octahedral calcium layer of T_{14}; $T_{14}^{Si_t}$/GS: GS interfacing with the tetrahedral silicate layer of T_{14}].

developed at the interface between the T_{14} structures and the GS. While all the T_{14}/GS nanocomposites reached a similar fracture shear strength at fracture (4.9–5.3 GPa), the $T_{14}^{O_w}$/GS nanocomposite with the GS interfacing with water exhibited a much lower fracture strain than the two other nanocomposites. During shear deformation, the $T_{14}^{O_w}$/GS nanocomposite displayed a more rapid build-up in shear strength, which resulted in an earlier fracture (i.e., at a lower strain) of the GS than observed for the $T_{14}^{Ca_o}$/GS and $T_{14}^{Si_t}$/GS nanocomposites. The GS in the $T_{14}^{O_w}$/GS nanocomposite failed abruptly before the failure of the T_{14} structure, resulting in a brittle fracture of the nanocomposite, followed by a subsequent plastic behavior. Even after failure, the T_{14} structure was able to withstand some of the load. The plastic behavior was attributed to the internal displacements and rotations of the atoms in the silicate tetrahedral and calcium octahedral layers of the T_{14} structure. The water molecules at the surface of the T_{14} structure were thought to have promoted molecular friction with the GS, building up stresses at the surface of the GS that were greater than the GS intrinsic capability to resist friction, thus causing the GS to fail at a strain lower than its intrinsic fracture shear strain and before the failure of the T_{14} matrix. The water molecules rotated during shear to release stress because of their reduced mobility (confined space of the interface) and the hydrophobic effect of the GS (entropy-driven), thus ripping the GS. In contrast, for the nanocomposites with the dry solid surfaces (calcium and silicate) interfacing with the GS, the shear stress initially increased at a lower rate, and the nanocomposites exhibited a more gradual failure. The shear strain caused distortion of the tetrahedral and octahedral sheets of the T_{14} matrix, in addition to ∠C–C–C angle bending and

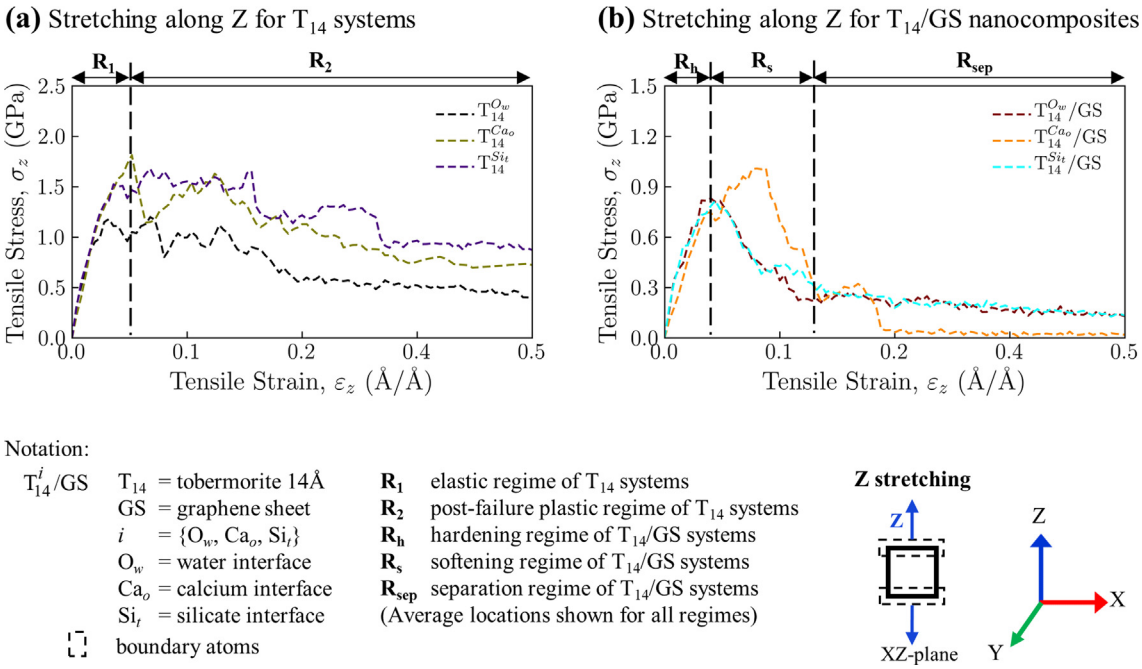

Fig. 10. Stress–strain response for out-of-plane (Z-direction) tensile loading of (a) T_{14} systems and (b) T_{14}/GS nanocomposites. [$T_{14}^{O_w}$: T_{14} structure with exposed water layer surface; $T_{14}^{Ca_o}$: T_{14} structure with exposed octahedral calcium surface; $T_{14}^{Si_t}$: T_{14} structure with exposed tetrahedral silicate surface; $T_{14}^{O_w}$/GS: GS interfacing with the bottom surface water of T_{14}; $T_{14}^{Ca_o}$/GS: GS interfacing with the octahedral calcium layer of T_{14}; $T_{14}^{Si_t}$/GS: GS interfacing with the tetrahedral silicate layer of T_{14}].

C–C–C–C dihedral bending of the GS. The shear stress increased initially due to the load being shared by both the T_{14} structure and the GS up to failure of the T_{14} structure at which point the stress increased gradually due to the GS loading regime and plastic behavior of the T_{14} structure until failure of the GS, which occurred at its intrinsic fracture shear strain (i.e., *ca.* 0.321 [28]). The interaction energy as a function of shear loading was 2–3 times greater (more negative) for the water interface compared to the calcium and silicate interfaces (Fig. 14), which was consistent with the higher rate of strength development and greater molecular friction forces exerted by the water molecules on the GS compared to that with the dry solid surfaces (calcium and silicate). As discussed in section 3.1.1, the role of water in enhancing molecular friction between two surfaces has been reported in the literature [66,67,69,70].

3.1.4. Strain energy density

The strain energy density indirectly measured the toughness of the T_{14}/GS nanocomposites. The GS significantly enhanced the in-plane tensile and shear toughness of the T_{14} systems, providing the nanocomposites with a greater resistance to fracture. The strain energy densities of the T_{14}/GS nanocomposites were *ca.* 3–18 times greater under in-plane tensile loading and *ca.* 3–5 times greater under shear deformation than their respective T_{14} systems with no GS reinforcement (Table 1). Under in-plane tensile loading, the T_{14}/GS nanocomposites showed a greater resistance to fracture in the X-direction (strain energy density *ca.* 2 times greater than in the Y-direction) contrary to the T_{14} systems with no GS reinforcement that showed a greater resistance to fracture in the Y-direction (direction of greater linear density of atoms). This result was primarily attributed to the large fracture shear strain of the GS [28,71,72] and demonstrated the role of the GS orientation (the most stretchable direction of the GS was along the X-direction) in controlling the tensile toughness of the nanocomposites.

The influence of the water interface versus dry solid interface on the T_{14}/GS nanocomposite toughness was apparent with a greater strain energy density under tension for the $T_{14}^{O_w}$/GS nanocomposite with the GS interfacing with water and a lower strain energy density under shear compared to the nanocomposites with the dry solid surfaces (calcium and silicate) interfacing with the GS. This behavior correlated with greater molecular friction forces promoted by the water interface and was in agreement with a similar effect of liquid interfaces reported in the literature [67,69]. The in-plane tensile strain energy density of the $T_{14}^{O_w}$/GS nanocomposite with the GS interfacing with water was *ca.* 1.3 times greater in the X- and Y-directions than that of the nanocomposites with the GS interfacing with the calcium and silicate surfaces. The shear strain energy density of the T_{14}/GS nanocomposites with the GS interfacing with the calcium and silicate surfaces was approximately twice that of the nanocomposite with the water interface.

In contrast, under out-of-plane (Z-direction) tensile loading, the in-plane GS reinforcement led to a lower resistance to fracture of the nanocomposites with the GS interfacing with the water and silicate surfaces (strain energy densities *ca.* 3 and *ca.* 4 times lower, respectively) and similar resistance to fracture for the nanocomposite with the GS interfacing with the calcium surface as a result of the weak interaction of the GS with the T_{14} systems.

3.2. Elastic moduli, shear moduli, bulk moduli, and linear compressibility

3.2.1. In-plane elastic and shear moduli

The in-plane elastic behavior of the T_{14} systems was affected by the differences in the stacking and exposure of the calcium, silicate, and water layers within each structure at equilibrium. These differences in structural layer build-up (different representative volume elements, RVE) affected the initial local stress distribution at equilibrium within the structures and resulted in higher stiffness and elastic anisotropy of the T_{14} structures with the exposed calcium and silicate surfaces ($T_{14}^{Ca_o}$ and $T_{14}^{Si_t}$, respectively) compared to the T_{14} structure with the exposed water surface ($T_{14}^{O_w}$), which exhibited a smaller stiffness and similar intrinsic, in-plane elastic mod-

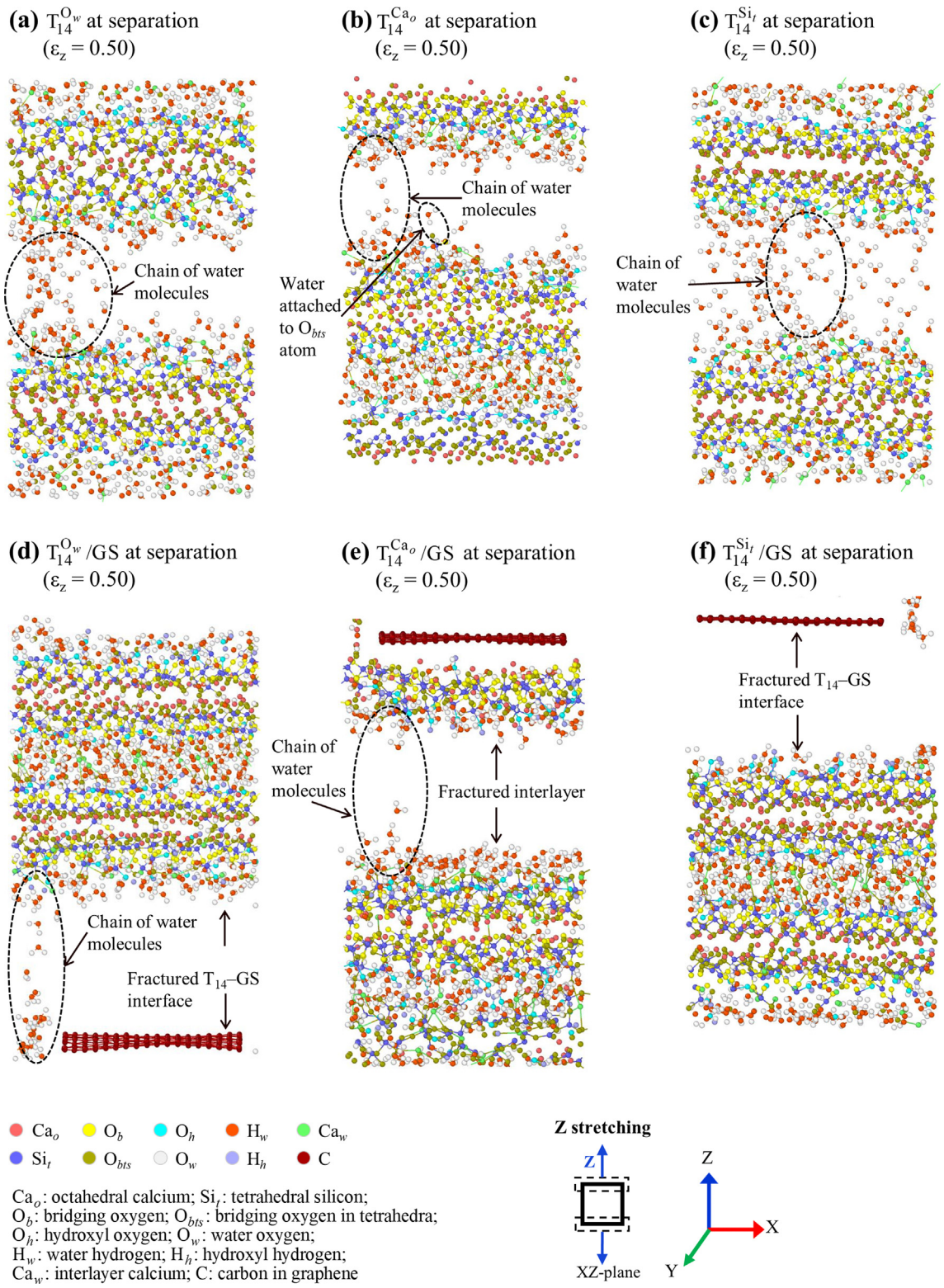

Fig. 11. Separation stage of T_{14} systems and T_{14}/GS nanocomposites during out-of-plane tensile loading along the Z-direction: (a) T_{14} structure with exposed water surface ($T_{14}^{O_w}$); (b) T_{14} structure with exposed octahedral calcium surface ($T_{14}^{Ca_o}$); (c) T_{14} structure with exposed tetrahedral silicate surface ($T_{14}^{Si_t}$); (d) nanocomposite with the GS interfacing with the bottom surface water of T_{14} ($T_{14}^{O_w}$/GS); (e) nanocomposite with the GS interfacing with the octahedral calcium layer of T_{14} ($T_{14}^{Ca_o}$/GS); and (f) nanocomposite with the GS interfacing with the tetrahedral silicate layer of T_{14} ($T_{14}^{Si_t}$/GS).

ulus values in all directions (*ca.* 49 GPa), indicating that the $T_{14}^{O_w}$ structure was elastically quasi-isotropic (Fig. 15a). The most elastic anisotropy was seen for the T_{14} structure with the exposed calcium surface with the greatest intrinsic stiffness along the 45-225° and 135-315° (i.e., ⟨1 1 0⟩ family) directions and the lowest intrinsic stiffness along the X-direction. The intrinsic elastic modulus values of the T_{14} systems ranged from 48.9 to 66.7 GPa in the X-direction and 49.0–74.0 GPa in the Y-direction, which compared well overall

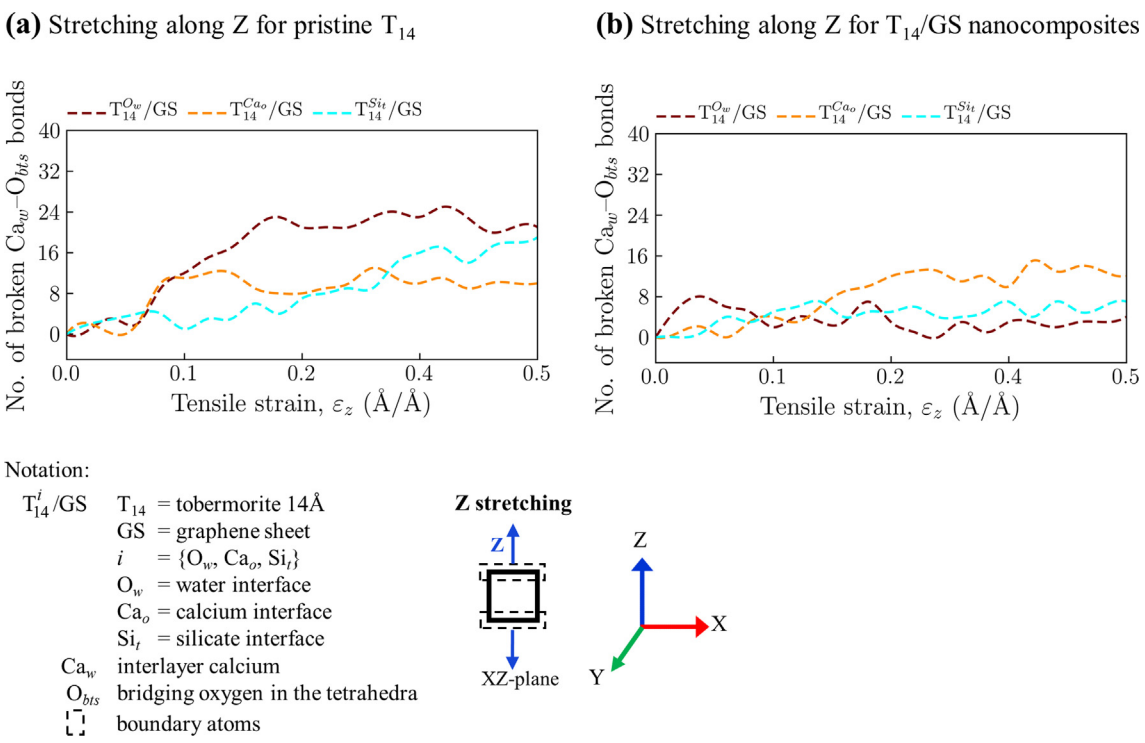

Fig. 12. Evolution of the number of broken Ca_w–O_{bts} bonds as a function of applied strain during out-of-plane (Z-direction) tensile loading of (a) the T_{14} systems and (b) the T_{14}/GS nanocomposites. [$T_{14}^{O_w}$: T_{14} structure with exposed water layer surface; $T_{14}^{Ca_o}$: T_{14} structure with exposed octahedral calcium surface; $T_{14}^{Si_t}$: T_{14} structure with exposed tetrahedral silicate surface; $T_{14}^{O_w}$/GS: GS interfacing with the bottom surface water of T_{14}; $T_{14}^{Ca_o}$/GS: GS interfacing with the octahedral calcium layer of T_{14}; $T_{14}^{Si_t}$/GS: GS interfacing with the tetrahedral silicate layer of T_{14}].

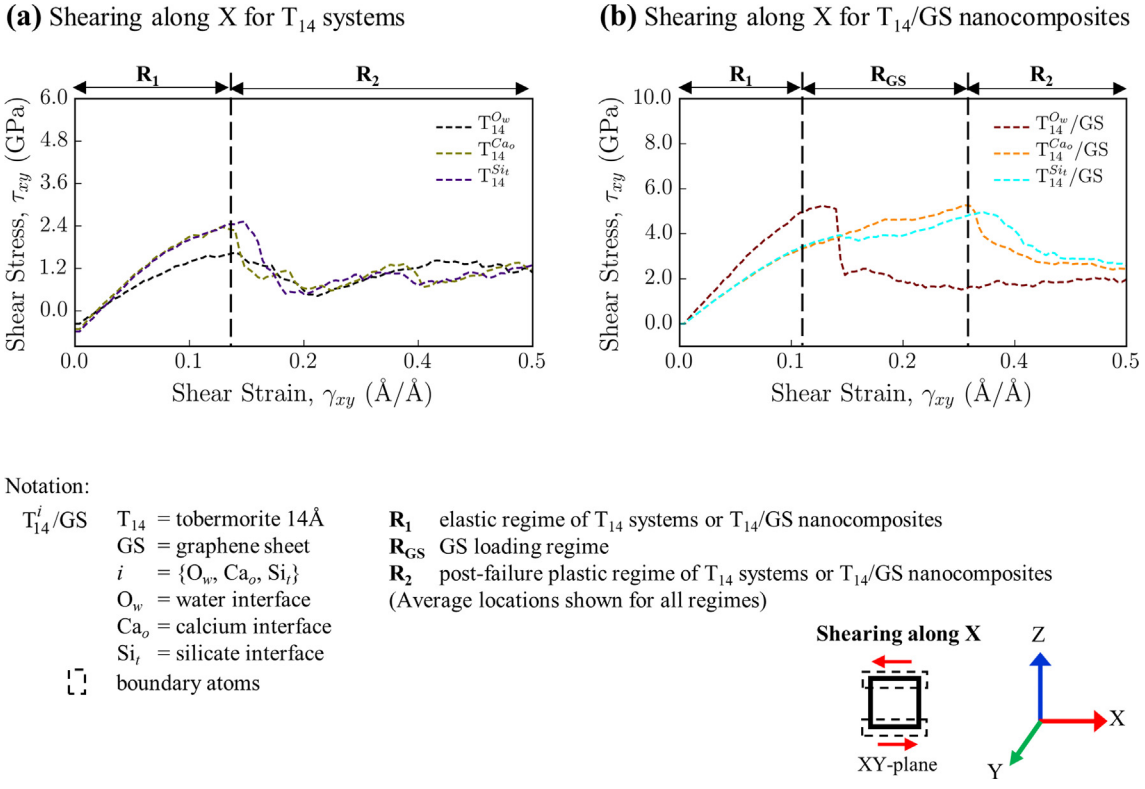

Fig. 13. Shear stress–strain evolution of the (a) T_{14} systems and (b) T_{14}/GS nanocomposites under shear loading along the X-direction. [$T_{14}^{O_w}$: T_{14} structure with exposed water layer surface; $T_{14}^{Ca_o}$: T_{14} structure with exposed octahedral calcium surface; $T_{14}^{Si_t}$: T_{14} structure with exposed tetrahedral silicate surface; $T_{14}^{O_w}$/GS: GS interfacing with the bottom surface water of T_{14}; $T_{14}^{Ca_o}$/GS: GS interfacing with the octahedral calcium layer of T_{14}; $T_{14}^{Si_t}$/GS: GS interfacing with the tetrahedral silicate layer of T_{14}].

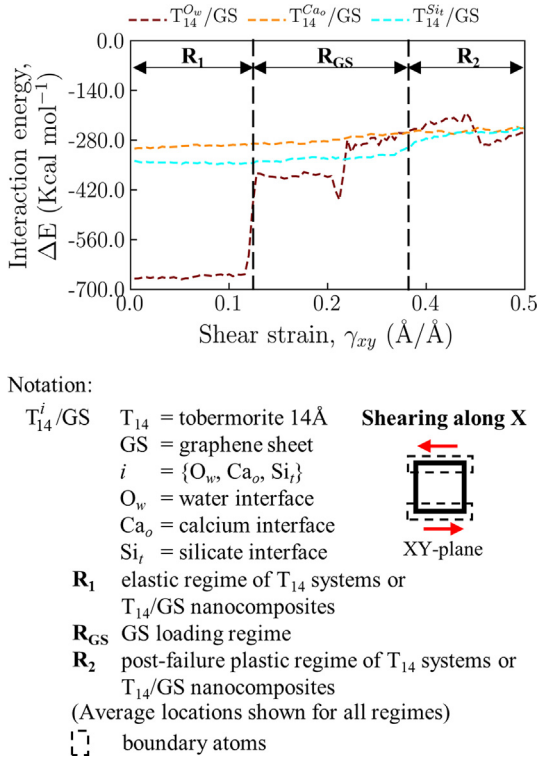

Fig. 14. Energy of interaction between the tobermorite 14 Å (T_{14}) structures and the graphene sheet (GS) as a function of strain during shear loading along the X-direction. [$T_{14}^{O_w}$/GS: GS interfacing with the bottom surface water of T_{14}; $T_{14}^{Ca_o}$/GS: GS interfacing with the octahedral calcium layer of T_{14}; $T_{14}^{Si_t}$/GS: GS interfacing with the tetrahedral silicate layer of T_{14}].

with values from atomistic studies that range from 25.0 to 69.0 GPa [9,12,51–53,73–78] but were, however, higher than experimental values obtained from nanoindentation of low and high density C–S–H, which range from 18.2 to 41.5 GPa [79–84]. The higher values from the MD simulations were consistent with the nanoscale size, defect free structure, and infinite silicate chain length of the T_{14}-like C–S–H models compared to real experimental systems.

The GS enhanced the intrinsic (equilibrium, zero strain) in-plane elastic modulus of the T_{14} systems by a factor of *ca.* 2 while decreasing (i.e., flattening) the out-of-plane elastic modulus of the T_{14} systems as seen from the 3-dimensional, disk-shaped region of the directional elastic modulus values in Fig. 16. The GS interacted weakly in the [0 0 1] direction with the T_{14} matrix via van der Waals interaction, which was responsible for the small out-of-plane elastic modulus of the T_{14}/GS nanocomposites. The GS imparted the higher stiffness to the T_{14}/GS nanocomposites while the T_{14} matrix imparted elastic anisotropy as seen by the deviation from the circular shape of the directional intrinsic elastic modulus (Fig. 15b). The T_{14}/GS nanocomposite with the GS interfacing with the tetrahedral silicate surface exhibited the most elastic anisotropy with a greater value lobe of the intrinsic elastic modulus (greatest stiffness) along the Y-direction and the lowest intrinsic elastic modulus value (lowest stiffness) along the 45-225° and 135-315° (i.e., ⟨1 1 0⟩ family) directions. The greater stiffness in the Y-direction was the combined result of the AC direction (stiffer direction) of the GS and running silicate chain of the T_{14} matrix (greater linear density) along the Y-direction.

The influence of the interface between the T_{14} matrix and the GS on the in-plane elastic modulus of the nanocomposites was revealed upon loading by a change in stiffness behavior that was accompanied by a reduction in the nanocomposite elastic modulus (Fig. 15b and c). The non-linear behavior of the elastic modulus as a function of strain resulted in an effective modulus that was lower than the intrinsic modulus (i.e., modulus at equilibrium before loading). During the elastic loading stage, the effect of the GS reinforcement was controlled by the stiffness of the GS and the interactions between the GS and the T_{14} matrix. Similar effective in-plane elastic modulus values were seen in all directions for each respective nanocomposite, indicating that upon loading, the nanocomposites became elastically quasi-isotropic (Fig. 15c). Under load, a greater reduction in the elastic modulus (i.e., stiffness) was seen in all directions for the nanocomposites with the calcium and silicate interfaces compared to that of the nanocomposite with the water interface, resulting in a greater effective elastic modulus (i.e., effective stiffness) for the nanocomposite with the water interface and lower but similar effective elastic modulus values for the nanocomposites with the calcium and silicate interfaces with respect to their respective intrinsic values. During loading, the surface friction between the water molecules and the GS were thought to have dominated, thus leading to a greater stiffness of the nanocomposites compared to that seen when the GS interacted with the dry, solid surfaces. The decrease in stiffness for the nanocomposites with the calcium and silicate interfaces relative to their respective intrinsic stiffness (i.e., at equilibrium before loading) was attributed primarily to a reorientation of the atoms within the T_{14} matrix occurring during loading.

Like for the in-plane elastic modulus, the GS increased the shear modulus of the T_{14} systems (Fig. 17). The influence of the interface between the T_{14} matrix and the GS was apparent for the nanocomposites with the GS interfacing with water. While the T_{14} system with the exposed water surface exhibited a lower shear modulus compared to the T_{14} systems with the exposed calcium and silicate surfaces because of a higher water content within the structure, the GS reinforced nanocomposite with the water interface (i.e., $T_{14}^{O_w}$/GS) showed the highest shear modulus, demonstrating the prominent effect of the water interface and molecular friction forces during shear loading. In contrast, the nanocomposites with the GS interfacing with the calcium and silicate surfaces (i.e., $T_{14}^{Ca_o}$/GS and $T_{14}^{Si_t}$/GS) had similar shear modulus values.

3.2.2. Bulk moduli and linear compressibility

A greater bulk modulus (resistance to compression) and thus lower volume compressibility were observed for the T_{14} system with the exposed water surface ($T_{14}^{O_w}$) while a lower bulk modulus

Table 1
Strain energy densities of the T_{14} systems and T_{14}/GS nanocomposites calculated from the tensile (in-plane and out-of-plane) and shear stress–strain responses.

Systems	Tensile (Γ), X ($\times 10^9$ J m^{-3})	Tensile (Γ), Y ($\times 10^9$ J m^{-3})	Tensile (Γ), Z ($\times 10^9$ J m^{-3})	Shear (Π), XY ($\times 10^9$ J m^{-3})
$T_{14}^{O_w}$	0.139	0.194	0.079	0.148
$T_{14}^{Ca_o}$	0.090	0.287	0.072	0.186
$T_{14}^{Si_t}$	0.096	0.239	0.107	0.239
$T_{14}^{O_w}$/GS	2.020	1.050	0.026	0.473
$T_{14}^{Ca_o}$/GS	1.525	0.781	0.074	0.845
$T_{14}^{Si_t}$/GS	1.520	0.837	0.029	0.877

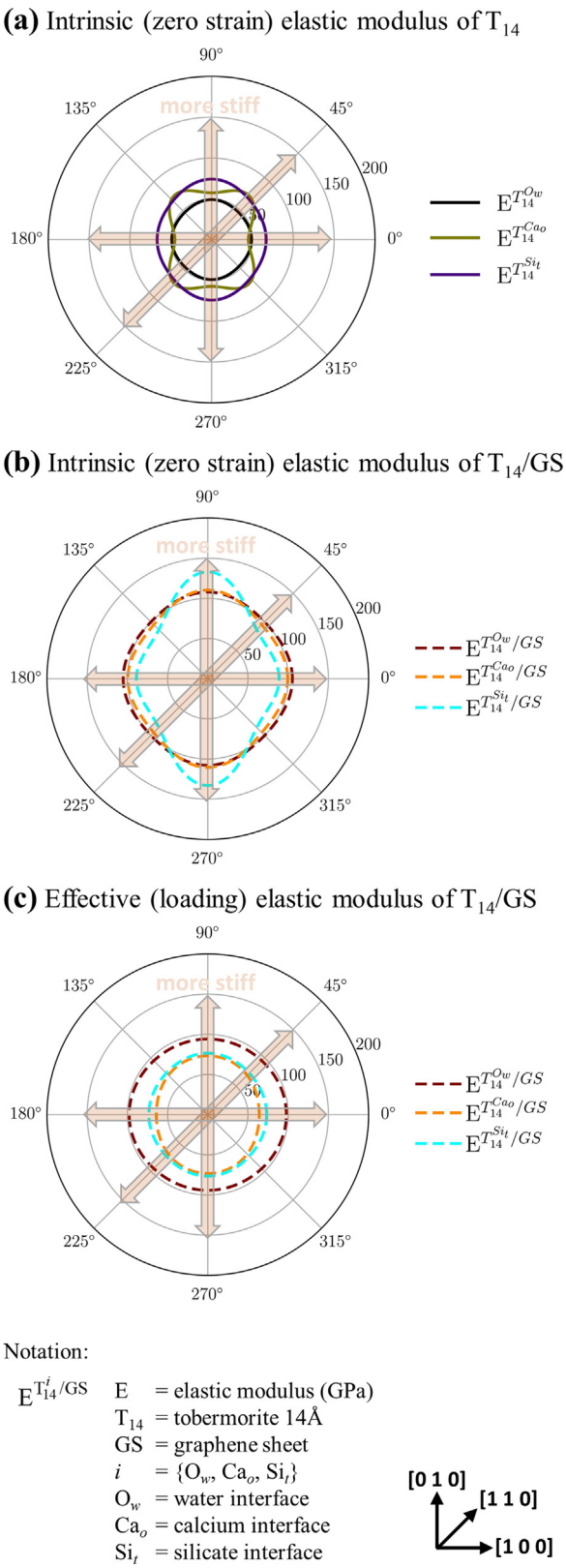

Fig. 15. 2D plots of the directional in-plane elastic modulus: (a) intrinsic elastic modulus of the T_{14} systems, (b) intrinsic elastic modulus of the T_{14}/GS nanocomposites, and (c) effective (elastic loading stage) elastic modulus of the T_{14}/GS nanocomposites. [$T_{14}^{O_w}$: T_{14} structure with exposed water layer surface; $T_{14}^{Ca_o}$: T_{14} structure with exposed octahedral calcium surface; $T_{14}^{Si_t}$: T_{14} structure with exposed tetrahedral silicate surface; $T_{14}^{O_w}$/GS: GS interfacing with the bottom surface water of T_{14}; $T_{14}^{Ca_o}$/GS: GS interfacing with the octahedral calcium layer of T_{14}; $T_{14}^{Si_t}$/GS: GS interfacing with the tetrahedral silicate layer of T_{14}].

and thus greater volume compressibility were observed for the T_{14} system with the exposed calcium octahedral surface ($T_{14}^{Ca_o}$) (Table 2). These differences in bulk modulus values were attributed to their differences in crystal structure assembly (i.e., stacking of the octahedral calcium, tetrahedral silicate, and water layers), which was consistent with results reported in the literature using high-pressure synchrotron X-ray diffraction [85] that indicated that the bulk modulus of tobermorite 14 Å was dominated by the incompressibility (i.e., stiffness) of the structure in the Z-direction. The bulk modulus value of the T_{14} system with the exposed water surface (34.0 GPa) compared well with values reported in the literature from atomistic modeling and experiments that range from 33.7 to 47.8 GPa [73–76,84–86]. The low value of the bulk modulus seen for the T_{14} system with the exposed octahedral surface (30.1 GPa) was thought to be due to structural defects in the silicate chain caused by the removal of the top silicate layer.

The GS reduced the bulk modulus of the T_{14} system with the exposed octahedral calcium and tetrahedral silicate surfaces (by *ca.* 15% and 9%, for the $T_{14}^{Ca_o}$/GS and $T_{14}^{Si_t}$/GS nanocomposites respectively; Table 2). The weak out-of-plane stiffness of the GS was thought to be responsible for the decrease in the bulk modulus. In contrast, for the nanocomposite with the GS interfacing with the water ($T_{14}^{O_w}$/GS nanocomposite), the GS did not reduce the bulk modulus of the nanocomposite because of the presence of the confined water molecules at the interface with the GS, which provided stiffness in the Z-direction of the nanocomposite (the out-of-plane stiffness was greater for the $T_{14}^{O_w}$/GS nanocomposite with the water interface than the $T_{14}^{Ca_o}$/GS and $T_{14}^{Si_t}$/GS nanocomposites with the solid interfaces).

The linear compressibility was affected by the amount of water within the T_{14} matrix and the structure of the interface between the T_{14} matrix and the GS (Fig. 18).

A greater compressibility in the Y-direction was observed for the T_{14} matrix that had the highest water content (i.e., $T_{14}^{O_w}$ with a water to silicon ratio of 1.66). In contrast, the T_{14} systems with the exposed calcium and silicate surfaces had less water and more solids (i.e., water to silicon ratio of 1.58 and 1.5 for $T_{14}^{Ca_o}$ and $T_{14}^{Si_t}$, respectively) and were thus less compressible along the direction of the running silicate chains. A strong anisotropy of the linear compressibility was observed for the T_{14} matrix with the exposed octahedral calcium surface ($T_{14}^{Ca_o}$) with a greater compressibility along the X-direction and lower compressibility along the Y-direction, as shown from the high value lobes along the X-direction (Fig. 18a). There was, however, no significant spatial dependence of the linear compressibility in the XY-plane (i.e., quasi-circular shape) for the T_{14} systems with the exposed water and tetrahedral silicate surfaces (i.e., $T_{14}^{O_w}$ and $T_{14}^{Si_t}$, respectively). The anisotropy in linear compressibility for the $T_{14}^{Ca_o}$ matrix resulted from its structural differences in the crystal structure assembly compared to the base T_{14} structure (i.e., T_{14} system with the exposed water surface, $T_{14}^{O_w}$) that were more prominent than for the T_{14} system with the exposed tetrahedral silicate surface ($T_{14}^{Si_t}$).

The GS significantly reduced the intrinsic (equilibrium, zero strain) linear compressibility of all T_{14} systems by *ca.* 45% in all directions of the XY plane by providing stiffness (the GS possesses extraordinary stiffness in both the ZZ and AC directions and a very low compressibility with a value of 0.00084 GPa^{-1} [28]). The spatial dependence of the intrinsic linear compressibility of the T_{14}/GS nanocomposites, however, remained conserved (i.e., similar shape of the directional compressibility than their respective pristine systems with no GS reinforcement), indicating that the linear compressibility was modulated by the structure of the T_{14} systems.

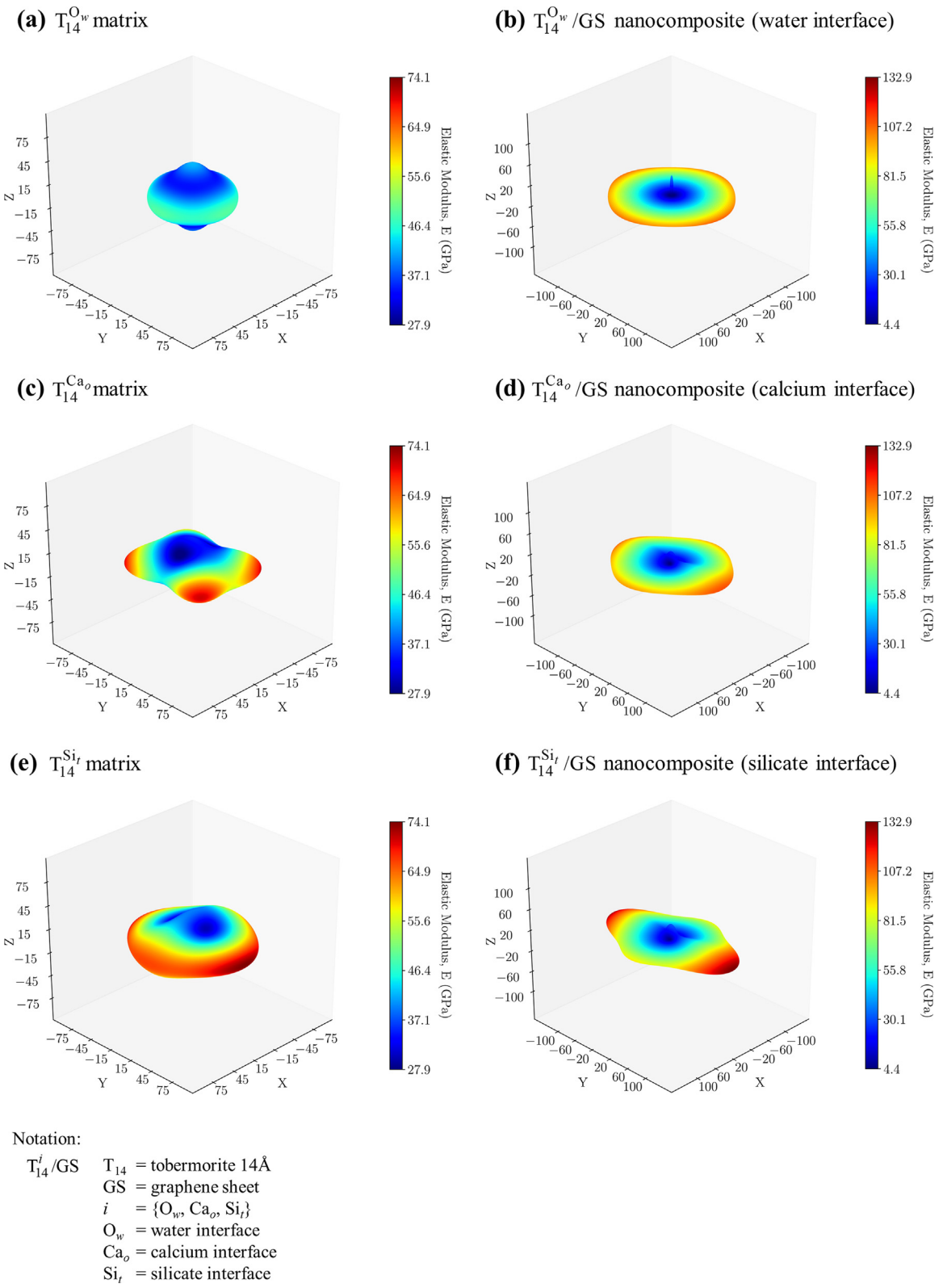

Fig. 16. 3D plots of the directional intrinsic elastic modulus of (a), (c), and (e) tobermorite 14 Å (T_{14}) systems with the exposed water layer ($T_{14}^{O_w}$), octahedral calcium ($T_{14}^{Ca_o}$), and tetrahedral silicate surfaces ($T_{14}^{Si_t}$), respectively and (b), (d), and (f) graphene sheet (GS) reinforced tobermorite 14 Å nanocomposites with the GS interfacing with the bottom surface water of T_{14} ($T_{14}^{O_w}$/GS), octahedral calcium layer ($T_{14}^{Ca_o}$/GS), and tetrahedral silicate layer ($T_{14}^{Si_t}$/GS), respectively.

Under load (strain of 0.025), the T_{14}/GS nanocomposites exhibited a change in their compressibility behavior (Fig. 18c) that was accompanied by an increase in compressibility relative to the nanocomposite intrinsic compressibility at zero strain. The linear compressibility of the nanocomposites increased due to the increase in bond lengths during loading of the calcium octahedral

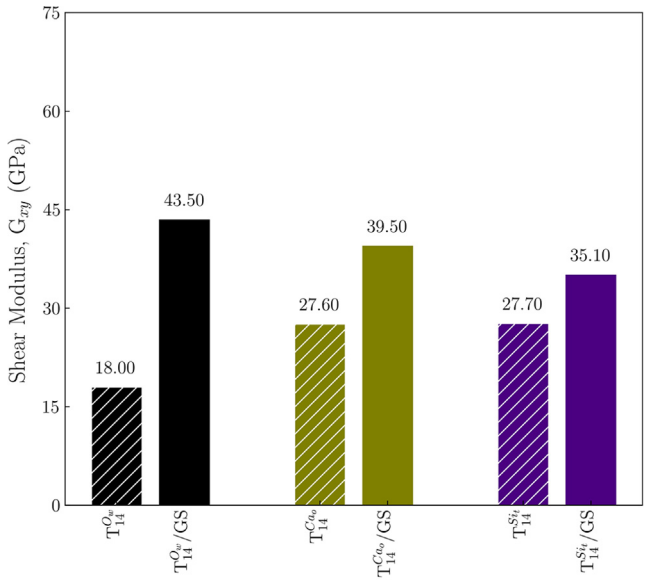

Notation:

T_{14}^{i}/GS
T_{14} = tobermorite 14Å
GS = graphene sheet
i = {O_w, Ca_o, Si_t}
O_w = water interface
Ca_o = calcium interface
Si_t = silicate interface

Fig. 17. Shear modulus for applied load in the XY plane along the X-direction for the T_{14} systems and T_{14}/GS nanocomposites. [$T_{14}^{O_w}$: T_{14} structure with exposed water layer surface; $T_{14}^{Ca_o}$: T_{14} structure with exposed octahedral calcium surface; $T_{14}^{Si_t}$: T_{14} structure with exposed tetrahedral silicate surface; $T_{14}^{O_w}$/GS: GS interfacing with the bottom surface water of T_{14}; $T_{14}^{Ca_o}$/GS: GS interfacing with the octahedral calcium layer of T_{14}; $T_{14}^{Si_t}$/GS: GS interfacing with the tetrahedral silicate layer of T_{14}].

Table 2
Volume compressibility and bulk moduli for the T_{14} systems and T_{14}/GS nanocomposites.

Systems	Volume Compressibility β_V (GPa^{-1})	Bulk Modulus κ (GPa)
$T_{14}^{O_w}$	0.029	34.0
$T_{14}^{Ca_o}$	0.033	30.1
$T_{14}^{Si_t}$	0.031	32.4
$T_{14}^{O_w}$/GS	0.028	35.0
$T_{14}^{Ca_o}$/GS	0.039	25.6
$T_{14}^{Si_t}$/GS	0.034	29.6

Notations:
$T_{14}^{O_w}$: T_{14} structure with exposed water layer surface.
$T_{14}^{Ca_o}$: T_{14} structure with exposed octahedral calcium surface.
$T_{14}^{Si_t}$: T_{14} structure with exposed tetrahedral silicate surface.
$T_{14}^{O_w}$/GS: GS interfacing with the bottom surface water of T_{14}.
$T_{14}^{Ca_o}$/GS: GS interfacing with the octahedral calcium layer of T_{14}.
$T_{14}^{Si_t}$/GS: GS interfacing with the tetrahedral silicate layer of T_{14}.

and silicate tetrahedral chains in the T_{14} matrix and carbon bonds in the GS. The nanocomposite with the GS interfacing with the octahedral calcium surface (i.e., $T_{14}^{Ca_o}$/GS nanocomposite) showed the most significant change in compressibility behavior. While the $T_{14}^{Ca_o}$/GS nanocomposite exhibited at zero strain its lowest compressibility in the Y-direction, during loading, its compressibility in that direction was significantly increased. The linear compressibility of the $T_{14}^{Ca_o}$/GS nanocomposite became then relatively independent of the direction (quasi-circular shape of the directional

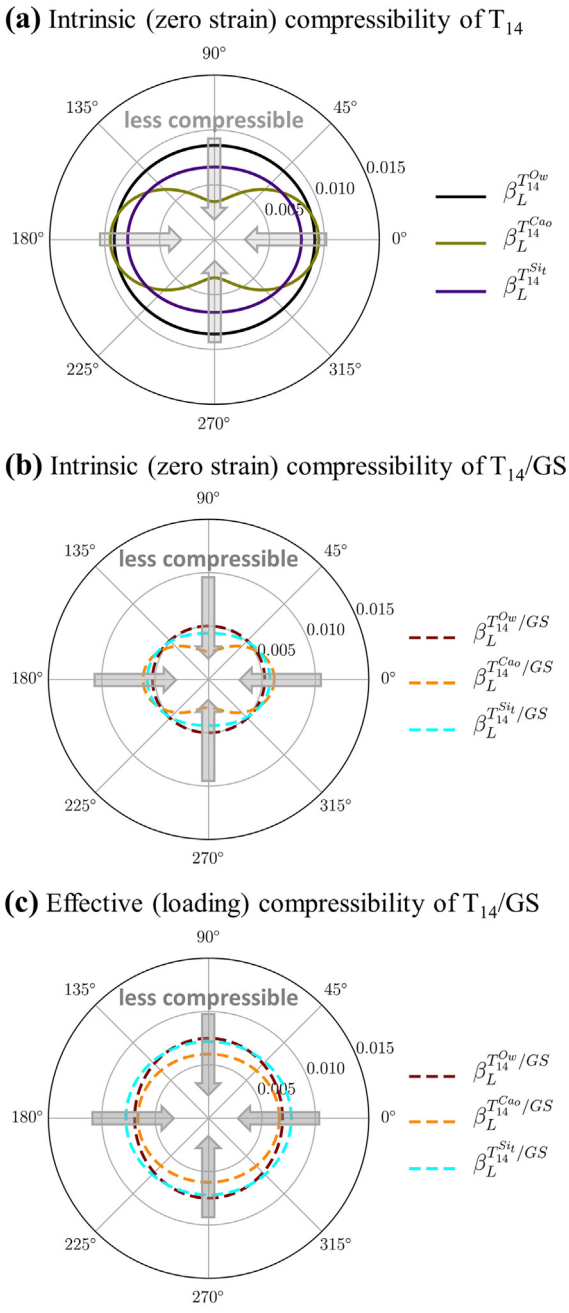

Notation:

$\beta_L^{T_{14}^{i}/GS}$
β_L = linear compressibility (GPa^{-1})
T_{14} = tobermorite 14Å
GS = graphene sheet
i = {O_w, Ca_o, Si_t}
O_w = water interface
Ca_o = calcium interface
Si_t = silicate interface

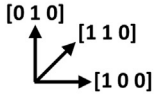

Fig. 18. 2D plots of the directional linear compressibility: (a) intrinsic linear compressibility of the T_{14} systems, (b) intrinsic linear compressibility of the T_{14}/GS nanocomposites, and (c) effective (elastic loading stage) linear compressibility of the T_{14}/GS nanocomposites. [$T_{14}^{O_w}$: T_{14} structure with exposed water layer surface; $T_{14}^{Ca_o}$: T_{14} structure with exposed octahedral calcium surface; $T_{14}^{Si_t}$: T_{14} structure with exposed tetrahedral silicate surface; $T_{14}^{O_w}$/GS: GS interfacing with the bottom surface water of T_{14}; $T_{14}^{Ca_o}$/GS: GS interfacing with the octahedral calcium layer of T_{14}; $T_{14}^{Si_t}$/GS: GS interfacing with the tetrahedral silicate layer of T_{14}].

linear compressibility). This change in compressibility behavior during loading demonstrated the influence of the structure of the interface between the T_{14} matrix and the GS. It was thought that, upon loading, the corrugated surface of the T_{14} system with the octahedral calcium surface (i.e., zigzag structure of the octahedral calcium layer) became flatter (i.e, stretching of the octahedral calcium chain) thus becoming more compressible.

4. Conclusions

The mechanical properties of tobermorite 14 Å-based structures reinforced with a single graphene sheet interfacing with three well-defined surfaces (i.e., bottom water layer, octahedral calcium layer, and tetrahedral silicate layer) were studied. The graphene sheet contributed to a significant increase in the XY-plane tensile and shear strengths, stiffness, and toughness of the tobermorite 14 Å-based structures. In-plane fracture tensile and shear strengths of the reinforced nanocomposites that were 180% to 360% and 90% to 225% greater, respectively, than those of the tobermorite 14 Å-based structures without the graphene sheet reinforcement as well as intrinsic in-plane elastic moduli that were twice that of the pristine structures could be realized. In contrast, the graphene sheet decreased the out-of-plane tensile strength capacity, stiffness, and bulk modulus of the tobermorite 14 Å-based structures because of the weak interaction of the graphene sheet with the structures. The influence of mediating water at the interface with the graphene sheet versus dry solid surfaces and of the structure of the solid surfaces (i.e., ordered octahedral calcium zigzag sheet versus tetrahedral silicate chain) on the overall nanocomposite behavior was revealed. The graphene sheet exhibited more apparent in-plane strengthening effect when interfacing with water than with either of the solid surfaces (i.e., calcium or silicate surfaces). The confined water molecules interfacing with the graphene sheet promoted surface friction during tensile and shear loading, thus leading to a greater fracture tensile strength, faster rate of shear strength development, and greater toughness under in-plane tensile loading but lower shear toughness compared to the nanocomposites with the dry, solid surfaces (calcium and silicate) interfacing with the graphene sheet. The results further demonstrated the role of the matrix structure in modulating the in-plane stiffness and linear compressibility of the nanocomposites at zero strain and the dominant role of the graphene sheet and interface between the graphene sheet and the matrix upon loading.

Declaration of Competing Interest

The authors declare that they have no known competing financial interests or personal relationships that could have appeared to influence the work reported in this paper.

Acknowledgements

This research was supported by the National Science Foundation under NSF CMMI 1462575. The authors would like also to thank the U.S Department of Energy funded Consortium for Risk Evaluation with Stakeholder Participation III (CRESP, Cooperative Agreement Number DE-FC01-06EW07053) for providing the computational resources. The authors also gratefully acknowledge Dr. Lesa Brown for her valuable assistance.

Appendix A. Supplementary data

Supplementary data to this article can be found online at https://doi.org/10.1016/j.conbuildmat.2019.117237.

References

[1] F. Faghih, D. Das, A. Ayoub, Seismic Behavior of Fiber Reinforced Steel-concrete Composite Systems, Proc. Eng. 171 (2017) 899–908, https://doi.org/10.1016/j.proeng.2017.01.386.
[2] H.F.W. Taylor, Cement Chemistry, Academic Press, London, 1990.
[3] L. Raki, J. Beaudoin, R. Alizadeh, J. Makar, T. Sato, Cement and concrete nanoscience and nanotechnology, Materials 3 (2) (2010) 918–942.
[4] F. Sanchez, K. Sobolev, Nanotechnology in concrete – A review, Constr. Build. Mater. 24 (11) (2010) 2060–2071, https://doi.org/10.1016/j.conbuildmat.2010.03.014.
[5] H. Yang, H. Cui, W. Tang, Z. Li, N. Han, F. Xing, A critical review on research progress of graphene/cement based composites, Compos. A Appl. Sci. Manuf. 102 (2017) 273–296, https://doi.org/10.1016/j.compositesa.2017.07.019.
[6] F.-J. Ulm, M. Vandamme, C. Bobko, J. Alberto Ortega, K. Tai, C. Ortiz, Statistical indentation techniques for hydrated nanocomposites: concrete, bone, and shale, J. Am. Ceramic Soc. 90 (9) (2007) 2677–2692, https://doi.org/10.1111/j.1551-2916.2007.02012.x.
[7] M. Reda Taha, E. Soliman, M. Sheyka, A. Reinhardt, M. Al-Haik, Fracture toughness of hydrated cement paste using nanoindentation, 2010.
[8] P. Faucon, J.M. Delaye, J. Virlet, Molecular dynamics simulation of the structure of calcium silicate hydrates: I. Ca4+xSi6O14+2x(OH)4–2x(H2O)2(0 ≤x≤ 1), J. Solid State Chem. 127 (1) (1996) 92–97, https://doi.org/10.1006/jssc.1996.0361.
[9] D. Hou, J. Zhang, Z. Li, Y. Zhu, Uniaxial tension study of calcium silicate hydrate (C–S–H): structure, dynamics and mechanical properties, Mater. Struct. 48 (11) (2015) 3811–3824, https://doi.org/10.1617/s11527-014-0441-1.
[10] H. Manzano, E. Masoero, I. Lopez-Arbeloa, H.M. Jennings, Shear deformations in calcium silicate hydrates, Soft Matter. 9 (30) (2013) 7333–7341, https://doi.org/10.1039/C3SM50442E.
[11] S.D. Palkovic, S. Yip, O. Büyüköztürk, Constitutive response of calcium-silicate-hydrate layers under combined loading, J. Am. Ceram. Soc. 100 (2) (2017) 713–723, https://doi.org/10.1111/jace.14628.
[12] D. Hou, T. Zhao, Z. Jin, H. Ma, Z. Li, Molecular simulation of calcium silicate composites: structure, dynamics, and mechanical properties, J. Am. Ceram. Soc. 98 (3) (2015) 758–769, https://doi.org/10.1111/jace.13368.
[13] M. Eftekhari, S. Mohammadi, Molecular dynamics simulation of the nonlinear behavior of the CNT-reinforced calcium silicate hydrate (C–S–H) composite, Compos. Part A: Appl. Sci. Manuf. 82 (Suppl. C) (2016) 78–87, https://doi.org/10.1016/j.compositesa.2015.11.039.
[14] D. Hou, Z. Lu, X. Li, H. Ma, Z. Li, Reactive molecular dynamics and experimental study of graphene-cement composites: structure, dynamics and reinforcement mechanisms, Carbon 115 (2017) 188–208, https://doi.org/10.1016/j.carbon.2017.01.013.
[15] M.F. Kai, L.W. Zhang, K.M. Liew, Graphene and graphene oxide in calcium silicate hydrates: chemical reactions, mechanical behavior and interfacial sliding, Carbon 146 (2019) 181–193, https://doi.org/10.1016/j.carbon.2019.01.097.
[16] D. Hou, T. Yang, J. Tang, S. Li, Reactive force-field molecular dynamics study on graphene oxide reinforced cement composite: functional group deprotonation, interfacial bonding and strengthening mechanism, PCCP 20 (13) (2018) 8773–8789, https://doi.org/10.1039/C8CP00006A.
[17] Z. Lu, D. Hou, L. Meng, G. Sun, C. Lu, Z. Li, Mechanism of cement paste reinforced by graphene oxide/carbon nanotubes composites with enhanced mechanical properties, RSC Adv. 5 (122) (2015) 100598–100605, https://doi.org/10.1039/C5RA18602A.
[18] Y. Zhang, T. Yang, Y. Jia, D. Hou, H. Li, J. Jiang, J. Zhang, Molecular dynamics study on the weakening effect of moisture content on graphene oxide reinforced cement composite, Chem. Phys. Lett. 708 (2018) 177–182, https://doi.org/10.1016/j.cplett.2018.08.023.
[19] D. Hou, T. Zhao, H. Ma, Z. Li, Reactive molecular simulation on water confined in the nanopores of the calcium silicate hydrate gel: structure, reactivity, and mechanical properties, J. Phys. Chem. C 119 (3) (2015) 1346–1358, https://doi.org/10.1021/jp509292q.
[20] B.A. Al Muhit, Investigation on the Mechanical, Microstructural, and Electrical Properties of Graphene Oxide-Cement Composite, Civil, Environmental, and Construction Engineering Electronic Theses and Dissertations, University of Central Florida, 2015.
[21] A. Kunhi Mohamed, S.C. Parker, P. Bowen, S. Galmarini, An atomistic building block description of C-S-H - Towards a realistic C-S-H model, Cem. Concr. Res. 107 (2018) 221–235, https://doi.org/10.1016/j.cemconres.2018.01.007.
[22] R.J.-M. Pellenq, A. Kushima, R. Shahsavari, K.J. Van Vliet, M.J. Buehler, S. Yip, F.-J. Ulm, A realistic molecular model of cement hydrates, Proc. Nat. Acad. Sci. 106 (38) (2009) 16102–16107, https://doi.org/10.1073/pnas.0902180106.
[23] L. Tao, R. Shahsavari, Diffusive, displacive deformations and local phase transformation govern the mechanics of layered crystals: the case study of

tobermorite, Sci. Rep. 7 (1) (2017) 5907, https://doi.org/10.1038/s41598-017-05115-4.
[24] W. Humphrey, A. Dalke, K. Schulten, VMD – Visual molecular dynamics, J. Mol. Graph. 14 (1996) 33–38.
[25] E. Bonaccorsi, S. Merlino, A.R. Kampf, The crystal structure of tobermorite 14 Å (Plombierite), a C-S–H phase, J. Am. Ceram. Soc. 88 (3) (2005) 505–512, https://doi.org/10.1111/j.1551-2916.2005.00116.x.
[26] A.I. Jewett, Z. Zhuang, J.-E. Shea, Moltemplate a coarse-grained model assembly tool, Biophys. J. 104 (2) (2013) 169a, https://doi.org/10.1016/j.bpj.2012.11.953.
[27] P. Dauber-Osguthorpe, V.A. Roberts, D.J. Osguthorpe, J. Wolff, M. Genest, A.T. Hagler, Structure and energetics of ligand binding to proteins: Escherichia coli dihydrofolate reductase-trimethoprim, a drug-receptor system, Proteins: Struct. Funct. Bioinf. 4 (1) (1988) 31–47, https://doi.org/10.1002/prot.340040106.
[28] B. Al-Muhit, F. Sanchez, Tunable mechanical properties of graphene by clustered line pattern hydroxyl functionalization via molecular dynamics simulations, Carbon 146 (2019) 680–700, https://doi.org/10.1016/j.carbon.2019.02.019.
[29] J.-L. Zang, Q. Yuan, F.-C. Wang, Y.-P. Zhao, A comparative study of Young's modulus of single-walled carbon nanotube by CPMD, MD and first principle simulations, Comput. Mater. Sci. 46 (3) (2009) 621–625, https://doi.org/10.1016/j.commatsci.2009.04.007.
[30] F. Sanchez, L. Zhang, Molecular dynamics modeling of the interface between surface functionalized graphitic structures and calcium–silicate–hydrate: interaction energies, structure, and dynamics, J. Colloid Interface Sci. 323 (2) (2008) 349–358, https://doi.org/10.1016/j.jcis.2008.04.023.
[31] F. Sanchez, L. Zhang, Interaction energies, structure, and dynamics at functionalized graphitic structure–liquid phase interfaces in an aqueous calcium sulfate solution by molecular dynamics simulation, Carbon 48 (4) (2010) 1210–1223, https://doi.org/10.1016/j.carbon.2009.11.044.
[32] P.M. Morse, Diatomic molecules according to the wave mechanics. II. Vibrational levels, Phys. Rev. 34 (1) (1929) 57–64, https://doi.org/10.1103/PhysRev.34.57.
[33] A.A. Skelton, P. Fenter, J.D. Kubicki, D.J. Wesolowski, P.T. Cummings, Simulations of the quartz(10$\bar{1}$1)/water interface: a comparison of classical force fields, Ab Initio molecular dynamics, and X-ray reflectivity experiments, J. Phys. Chem. C 115 (5) (2011) 2076–2088, https://doi.org/10.1021/jp109446d.
[34] R.T. Cygan, J.-J. Liang, A.G. Kalinichev, Molecular models of hydroxide, oxyhydroxide, and clay phases and the development of a general force field, J. Phys. Chem. B 108 (4) (2004) 1255–1266, https://doi.org/10.1021/jp0363287.
[35] J.P. Larentzos, J.A. Greathouse, R.T. Cygan, An ab Initio and classical molecular dynamics investigation of the structural and vibrational properties of talc and pyrophyllite, J. Phys. Chem. C 111 (34) (2007) 12752–12759, https://doi.org/10.1021/jp072959f.
[36] B. Fazelabdolabadi, A. Alizadeh-Mojarad, A molecular dynamics investigation into the adsorption behavior inside 001 kaolinite and 1014 calcite nano-scale channels: the case with confined hydrocarbon liquid, acid gases, and water, Appl. Nanosci. 7 (5) (2017) 155–165, https://doi.org/10.1007/s13204-017-0563-1.
[37] S.L. Teich-McGoldrick, J.A. Greathouse, R.T. Cygan, Molecular dynamics simulations of structural and mechanical properties of muscovite: pressure and temperature effects, J. Phys. Chem. C 116 (28) (2012) 15099–15107, https://doi.org/10.1021/jp303143s.
[38] G. Hantal, L. Brochard, H. Laubie, D. Ebrahimi, R.J.M. Pellenq, F.-J. Ulm, B. Coasne, Atomic-scale modelling of elastic and failure properties of clays, Mol. Phys. 112 (9–10) (2014) 1294–1305, https://doi.org/10.1080/00268976.2014.897393.
[39] J. Zhang, M. Pervukhina, M.B. Clennell, Nanoscale elastic properties of dry and wet smectite, Clays Clay Miner. 66 (3) (2018) 209–219, https://doi.org/10.1346/CCMN.2018.064094.
[40] J.L. Suter, P.V. Coveney, H.C. Greenwell, M.-A. Thyveetil, Large-scale molecular dynamics study of montmorillonite clay: emergence of undulatory fluctuations and determination of material properties, J. Phys. Chem. C 111 (23) (2007) 8248–8259, https://doi.org/10.1021/jp070294b.
[41] V.S. Vo, V.-H. Nguyen, S. Mahouche-Chergui, B. Carbonnier, D. Di Tommaso, S. Naili, From atomistic structure to thermodynamics and mechanical properties of epoxy/clay nanocomposites: investigation by molecular dynamics simulations, Comput. Mater. Sci. 139 (2017) 191–201, https://doi.org/10.1016/j.commatsci.2017.07.024.
[42] M. Mazo, L. Manevitch, N. Balabaev, A. Berlin, E.B. Gusarova, G. Rutledge, Temperature dependence of elastic properties of a pyrophyllite plate by molecular dynamics simulation, in: Proceedings of Second International Conference on Mathematical Modeling and Computer Simulation of Metal Technologies, MMT-2006. Israel, 2006, vol. 2, part 4, pp. 97–106, 2006.
[43] R.K. Mishra, A.K. Mohamed, D. Geissbühler, H. Manzano, T. Jamil, R. Shahsavari, A.G. Kalinichev, S. Galmarini, L. Tao, H. Heinz, R. Pellenq, A.C.T. van Duin, S.C. Parker, R.J. Flatt, P. Bowen, cemff: a force field database for cementitious materials including validations, applications and opportunities, Cem. Concr. Res. 102 (2017) 68–89, https://doi.org/10.1016/j.cemconres.2017.09.003.
[44] M.A. Mazo, L.I. Manevitch, E.B. Gusarova, M.Y. Shamaev, A.A. Berlin, N.K. Balabaev, G.C. Rutledge, Molecular dynamics simulation of thermomechanical properties of montmorillonite crystal. 1. Isolated clay nanoplate, J. Phys. Chem. B 112 (10) (2008) 2964–2969, https://doi.org/10.1021/jp076022q.
[45] J.E. Jones, S. Chapman, On the determination of molecular fields. - II. From the equation of state of a gas, Proc. R. Soc. London. Ser. A Containing Pap. Math. Phys. Charac. 106 (738) (1924) 463–477, https://doi.org/10.1098/rspa.1924.0082.
[46] S. Plimpton, Fast parallel algorithms for short-range molecular dynamics, J. Comput. Phys. 117 (1) (1995) 1–19, https://doi.org/10.1006/jcph.1995.1039.
[47] S. Nosé, A molecular dynamics method for simulations in the canonical ensemble, Mol. Phys. 52 (2) (1984) 255–268, https://doi.org/10.1080/00268978400101201.
[48] W.G. Hoover, Canonical dynamics: equilibrium phase-space distributions, Phys. Rev. A 31 (3) (1985) 1695–1697, https://doi.org/10.1103/PhysRevA.31.1695.
[49] H.A. Lorentz, Ueber die Anwendung des Satzes vom Virial in der kinetischen Theorie der Gase, Ann. Phys. 248 (1) (1881) 127–136, https://doi.org/10.1002/andp.18812480110.
[50] D. Berthelot, Sur le mélange des gaz, Comptes Rendus Hebdomadaires des Séances de l'Académie des Sciences 126 (1898) 1703–1855.
[51] D. Hou, Y. Zhu, Y. Lu, Z. Li, Mechanical properties of calcium silicate hydrate (C–S–H) at nano-scale: a molecular dynamics study, Mater. Chem. Phys. 146 (3) (2014) 503–511, https://doi.org/10.1016/j.matchemphys.2014.04.001.
[52] D. Hou, T. Zhao, P. Wang, Z. Li, J. Zhang, Molecular dynamics study on the mode I fracture of calcium silicate hydrate under tensile loading, Eng. Fract. Mech. 131 (Suppl. C) (2014) 557–569, https://doi.org/10.1016/j.engfracmech.2014.09.011.
[53] J. Fu, F. Bernard, S. Kamali-Bernard, Assessment of the elastic properties of amorphous calcium silicates hydrates (I) and (II) structures by molecular dynamics simulation, Mol. Simul. 44 (4) (2018) 285–299, https://doi.org/10.1080/08927022.2017.1373191.
[54] A.K. Subramaniyan, C.T. Sun, Continuum interpretation of virial stress in molecular simulations, Int. J. Solids Struct. 45 (14) (2008) 4340–4346, https://doi.org/10.1016/j.ijsolstr.2008.03.016.
[55] L. Sun, Y. Gao, Y. Li, K. Yoshida, T. Yano, D. Yi, Structural, bonding, anisotropic mechanical and thermal properties of Al4SiC4 and Al4Si2C5 by first-principles investigations, J. Asian Ceram. Soc. 4 (3) (2016) 289–298, https://doi.org/10.1016/j.jascer.2016.05.006.
[56] X.W. Zhou, T.W. Heo, B.C. Wood, V. Stavila, S. Kang, M.D. Allendorf, Finite-temperature behavior of PdHx elastic constants computed by direct molecular dynamics, Energy Convers. Manage. (2017), https://doi.org/10.1557/adv.2017.387.
[57] M.S. Stetsenko, Determining the elastic constants of hydrocarbons of heavy oil products using molecular dynamics simulation approach, J. Petrol. Sci. Eng. 126 (2015) 124–130, https://doi.org/10.1016/j.petrol.2014.12.021.
[58] F. Mouhat, F.-X. Coudert, Necessary and sufficient elastic stability conditions in various crystal systems, Physical Review B 90 (22) (2014) 224104.
[59] M. Born, K. Huang, Dynamical Theory of Crystal Lattices, Oxford University Press, London, 1962.
[60] Y. Zhou, D. Hou, G. Geng, P. Feng, J. Yu, J. Jiang, Insights into the interfacial strengthening mechanisms of calcium-silicate-hydrate/polymer nanocomposites, PCCP 20 (12) (2018) 8247–8266, https://doi.org/10.1039/C8CP00328A.
[61] J.J. Thomas, H.M. Jennings, A.J. Allen, Relationships between Composition and Density of Tobermorite, Jennite, and Nanoscale CaO–SiO2–H2O, J. Phys. Chem. C 114 (17) (2010) 7594–7601, https://doi.org/10.1021/jp910733x.
[62] D. Hou, H. Ma, Y. Zhu, Z. Li, Calcium silicate hydrate from dry to saturated state: structure, dynamics and mechanical properties, Acta Mater. 67 (2014) 81–94, https://doi.org/10.1016/j.actamat.2013.12.016.
[63] D. Hull, T.W. Clyne, An Introduction to Composite Materials, Cambridge University Press, Cambridge, UK, 1996.
[64] M. Youssef, R.J.M. Pellenq, B. Yildiz, Glassy nature of water in an ultraconfining disordered material: the case of calcium–silicate–hydrate, J. Am. Chem. Soc. 133 (8) (2011) 2499–2510, https://doi.org/10.1021/ja107003a.
[65] A. Schlaich, J. Kappler, R.R. Netz, Hydration friction in nanoconfinement: from bulk via interfacial to dry friction, Nano Lett. 17 (10) (2017) 5969–5976, https://doi.org/10.1021/acs.nanolett.7b02000.
[66] N. Dhopatkar, A.P. Defante, A. Dhinojwala, Ice-like water supports hydration forces and eases sliding friction, Sci. Adv. 2 (8) (2016), https://doi.org/10.1126/sciadv.1600763 e1600763.
[67] H. Lee, J.-H. Ko, J.S. Choi, J.H. Hwang, Y.-H. Kim, M. Salmeron, J.Y. Park, Enhancement of friction by water intercalated between graphene and mica, J. Phys. Chem. Lett. 8 (15) (2017) 3482–3487, https://doi.org/10.1021/acs.jpclett.7b01377.
[68] M. Lee, B. Kim, J. Kim, W. Jhe, Noncontact friction via capillary shear interaction at nanoscale, Nat. Commun. 6 (2015) 7359. https://www.nature.com/articles/ncomms8359#supplementary-information, https://doi.org/10.1038/ncomms8359.
[69] H. Cai, Y. Guo, W. Guo, Friction induced structural transformations of water monolayers at graphene/Cu interfaces, PCCP 20 (6) (2018) 4137–4143, https://doi.org/10.1039/C7CP08035B.
[70] E.K. Goharshadi, G. Akhlamadi, S.J. Mahdizadeh, Investigation of graphene oxide nanosheets dispersion in water based on solubility parameters: a molecular dynamics simulation study, RSC Adv. 5 (129) (2015) 106421–106430, https://doi.org/10.1039/C5RA19932H.
[71] K. Min, N.R. Aluru, Mechanical properties of graphene under shear deformation, Appl. Phys. Lett. 98 (1) (2011), https://doi.org/10.1063/1.3534787 013113.

[72] A. Hadizadeh Kheirkhah, E. Saeivar Iranizad, M. Raeisi, A. Rajabpour, Mechanical properties of hydrogen functionalized graphene under shear deformation: a molecular dynamics study, Solid State Commun. 177 (2014) 98–102, https://doi.org/10.1016/j.ssc.2013.10.004.
[73] R. Shahsavari, M.J. Buehler, R.J.M. Pellenq, F.-J. Ulm, First-principles study of elastic constants and interlayer interactions of complex hydrated oxides: case study of tobermorite and jennite, J. Am. Ceram. Soc. 92 (10) (2009) 2323–2330, https://doi.org/10.1111/j.1551-2916.2009.03199.x.
[74] H. Manzano, J.S. Dolado, A. Ayuela, Elastic properties of the main species present in Portland cement pastes, Acta Mater. 57 (5) (2009) 1666–1674, https://doi.org/10.1016/j.actamat.2008.12.007.
[75] H. Manzano, J.S. Dolado, A. Guerrero, A. Ayuela, Mechanical properties of crystalline calcium-silicate-hydrates: comparison with cementitious C-S-H gels, Physica Status Solidi A 204 (6) (2007) 1775–1780, https://doi.org/10.1002/pssa.200675359.
[76] R.J.-M. Pellenq, N. Lequeux, H. Van Damme, Engineering the bonding scheme in C-S-H: the iono-covalent framework, Cem. Concr. Res. 38 (2007) 159–174, https://doi.org/10.1016/j.cemconres.2007.09.026.
[77] M. Shirley, H. Bibian, Changes in the elastic moduli of C-S–H due to presence of interlaminar cations, Modell. Simul. Mater. Sci. Eng. 24 (3) (2016) 035018.
[78] S. Hajilar, B. Shafei, Molecular dynamics simulation of elastic properties of ordered CSH Gel: case study of tobermorite and jennite, Proceedings of the 5th International Symposium on Nanotechnology in Construction (NICOM-5), 2015.
[79] G. Constantinides, F.J. Ulm, K. Van Vliet, On the use of nanoindentation for cementitious materials, Mater. Struct. 36 (3) (2003) 191–196, https://doi.org/10.1007/BF02479557.
[80] G. Constantinides, F.-J. Ulm, The effect of two types of C-S-H on the elasticity of cement-based materials: results from nanoindentation and micromechanical modeling, Cem. Concr. Res. 34 (1) (2004) 67–80, https://doi.org/10.1016/S0008-8846(03)00230-8.
[81] F. Pelisser, P.J.P. Gleize, A. Mikowski, Effect of the Ca/Si molar ratio on the micro/nanomechanical Properties of Synthetic C-S-H measured by nanoindentation, J. Phys. Chem. C 116 (32) (2012) 17219–17227, https://doi.org/10.1021/jp302240c.
[82] H.M. Jennings, J.J. Thomas, J.S. Gevrenov, G. Constantinides, F.-J. Ulm, A multi-technique investigation of the nanoporosity of cement paste, Cem. Concr. Res. 37 (3) (2007) 329–336, https://doi.org/10.1016/j.cemconres.2006.03.021.
[83] J.J. Hughes, P. Trtik, Micro-mechanical properties of cement paste measured by depth-sensing nanoindentation: a preliminary correlation of physical properties with phase type, Mater. Charact. 53 (2) (2004) 223–231, https://doi.org/10.1016/j.matchar.2004.08.014.
[84] M. Vandamme, F.-J. Ulm, P. Fonollosa, Nanogranular packing of C-S–H at substochiometric conditions, Cem. Concr. Res. 40 (1) (2010) 14–26, https://doi.org/10.1016/j.cemconres.2009.09.017.
[85] J.E. Oh, S.M. Clark, H.-R. Wenk, P.J.M. Monteiro, Experimental determination of bulk modulus of 14Å tobermorite using high pressure synchrotron X-ray diffraction, Cem. Concr. Res. 42 (2) (2012) 397–403, https://doi.org/10.1016/j.cemconres.2011.11.004.
[86] A. Al-Ostaz, W. Wu, A.H.D. Cheng, C.R. Song, A molecular dynamics and microporomechanics study on the mechanical properties of major constituents of hydrated cement, Compos. B Eng. 41 (7) (2010) 543–549, https://doi.org/10.1016/j.compositesb.2010.06.005.